EFFECT OF INITIAL CONDITIONS ON THE COMPOUND SHEAR- AND BUOYANCY-DRIVEN MIXING

A Thesis

by

BETH ANN PLACETTE

Submitted to the Office of Graduate Studies of
Texas A&M University
in partial fulfillment of the requirements for the degree of

MASTER OF SCIENCE

August 2012

Major Subject: Mechanical Engineering

EFFECT OF INITIAL CONDITIONS ON THE COMPOUND SHEAR- AND BUOYANCY-DRIVEN MIXING

A Thesis

by

BETH ANN PLACETTE

Submitted to the Office of Graduate Studies of
Texas A&M University
in partial fulfillment of the requirements for the degree of

MASTER OF SCIENCE

Approved by:

Chair of Committee,	Devesh Ranjan
Committee Members,	Sharath Girimaji
	Junuthula Reddy
Head of Department,	Jerald Caton

August 2012

Major Subject: Mechanical Engineering

ABSTRACT

Effect of Initial Conditions on the Compound

Shear- and Buoyancy-driven Mixing. (August 2012)

Beth Ann Placette, B.S., Texas A&M University

Chair of Advisory Committee: Dr. Devesh Ranjan

The effect of initial conditions in combined shear- and buoyancy- driven mixing was investigated through the use of an implicit large eddy simulation code under active development at Los Alamos National Laboratory and Texas A&M University. Alterations were done over several months both at Los Alamos National Laboratory and at the Texas A&M University campus, and include a transition from tilted rig to convective channel arrangement, introduction of an inertial reference frame, alteration of boundary conditions, etc. This work resulted in the development of a numerical framework with the capability to model various shear and Atwood number arrangements such as those seen in an inertial confinement fusion environment.

In order to validate the code, it was compared to three published experiments, one with Atwood number 0.46, one with high Atwood number 0.6, and one with very low Atwood number 0.032. Upon validating the code, pure Rayleigh-Taylor and pure Kelvin-Helmholtz instabilities were modeled along with five intermediate cases of increasing shear and constant density gradient. Plots of mixing width, Richardson number, growth parameter, and molecular mixing were compared in order to determine

at what level of shear the minimum amount of mixing occurs. The results of height gradient and Reynolds number were to previous experiments and theory.

The least amount of molecular mixing at the centerline was found to be when the system had a low Atwood number (0.032) and a multimode initial interface perturbation. While the increase in modes of the interface perturbation did not result in a significant change in the growth parameter, the level of molecular mixing at the centerline substantially decreased. As shear was increased in the system, the mixing width and molecular mixing subsequently increased. For this reason, the shear in the system should be eliminated, or at least minimized, if at possible so as to prevent any additional amalgamation in the system. Analysis of the Reynolds number revealed that with an increase in velocity difference between the fluid layers, the value consequently increased. This trend matches with theoretical results as the value is a function of the mixing width and velocity, thus further validating the code. Analysis of the transitional Richardson number revealed that it had a smaller value in the computational case over the experiment, but this fact can be attributed the difference in mixing width between the two methods. The development of the numerical framework with the capability to model various shear and Atwood number arrangements offers the platform for future study of hydrodynamic instabilities.

To Mom and Dad

ACKNOWLEDGEMENTS

I would like to thank my research advisor Dr. Devesh Ranjan, who provided a great deal of support and guidance throughout these past two years. I would also like to send my immense gratitude to Dr. Malcolm Andrews for his insight into the computational code as well as all things mixing. Without his feedback, I would never have reached this point. I am very grateful for my committee members Dr. J. N. Reddy and Dr. Sharath Girimaji for their time and helpful comments. A big thanks goes out to my experimentalist coworkers for their help with ideas and insight into fluid mixing. Most of my knowledge on this subject was gained during in depth discussions with these fellows. In particular, I would like to thank Bhanesh Akula for his help with the gas channel experiment and computational replication, and for never getting annoyed with my endless questions. I would also like to send my gratitude to the other members of the Shock Tube Laboratory as well as all of the people I met during my summer at the Los Alamos National Laboratory Computational Physics Student Summer Workshop, particularly the coordinator Scott Runnels. These people have provided assistance both through discussion as well as distraction, and they have made the past two years more fun than one would expect from graduate school. Last but certainly not least I would like to thank my parents for their endless support through all of my endeavors. It was because of their continual encouragement throughout the years that I knew I could accomplish anything I set my mind to… except for touch the answer machine.

This research was supported in part by Los Alamos National Laboratory under subcontract number 87536-001-11.

TABLE OF CONTENTS

Page

Page

LIST OF FIGURES

FIGURE Page

FIGURE Page

FIGURE Page

FIGURE Page

FIGURE Page

1. INTRODUCTION

1.1 Overview and Motivation

Fluid mixing can be seen in a number of occurrences throughout the universe, from large scale structures such as super novas, to everyday items like water falling from a faucet, to micro-scale interactions such as inertial confinement fusion (ICF) capsules. With such a vast range of length and time scales over which the interaction can occur, the study of multi-material mixing is rather complex and underdeveloped. The presence of turbulence further complicates the matter, as nonlinearity and chaotic processes are introduced into the problem. These mixing instabilities can be split into three main categories: buoyancy-, shear-, and shock-driven turbulence. The first two have been a subject of interest for the better half of a century (Rayleigh 1883; Kelvin 1871), yet much is still left to be discovered. Current efforts are being made experimentally, numerically, and computationally to gain a better understanding of these phenomena (Smeeton & Youngs 1987; Youngs 1984; Dimonte & Schneider 2000; Banerjee & Andrews 2009).

The motivation behind this investigation comes primarily from the increased interest in ICF technology. This process involves the heating of a capsule filled with a combustible fluid, typically through the application of lasers. The increased temperature causes the external shell of the capsule to explode, creating an inward force which compresses the fuel. This inward motion, combined with subsequent shock waves,

---

This thesis follows the style of *Journal of Fluid Mechanics.*

compresses the fuel and causes ignition, releasing large amounts of energy in the process (Meyer-ter-Vehn 1999). The initial energy input can either be applied directly to the capsule (direct drive), or to an enclosure surrounding the capsule (indirect drive). Direct drive provides more energy, but is sensitive to the spatial quality of the laser beams, whereas indirect drive provides more uniform heating and is less prone to hydrodynamic instabilities (Lindl, McCrory, & Campbell 1992; Lindl 1995). For these reasons, the main focus of investigation for ICF has been heating with indirect drive. However, even with this method high-yield ICF is not currently obtainable due in part to the still present mixing within the capsule during the compression process. This fluid amalgamation acts to hinder the formation of a heat concentration at the center of the fuel cell, thus changing the yield and burn temperature and preventing the spatial density of the capsule from reaching the required value for combustion (Oron, Alon, & Shvarts 1998; Wilson *et al.* 2004). Of these hydrodynamic instabilities, the most prevalent and detrimental is the Rayleigh-Taylor buoyancy-driven instability and the subsequent Kelvin-Helmholtz shear-driven instability rollups (Keefe 1982; Kilkenny *et al.* 1994; Betti *et al.* 1998). Should it be possible to control these phenomena, and thus the level of mixing within the fuel capsule, high yield ICF could potentially be obtainable.

In order to control the interactions occurring within the capsule, the way in which the perturbations begin and grow must be fully understood. Many computational simulations have been used in an attempt to solve this problem, yet because of the elimination of important characteristics in the Reynolds-averaged-Navier-Stokes model and the computational requirement of direct numerical simulation, large eddy

simulation, and particularly implicit large eddy simulation, appears to be the best technique for modeling hydrodynamic instabilities (Moin & Mahesh 1998; Ristorcelli & Clark 2004; Grinstein, Margolin, & Rider 2007; Cheng 2009). The present effort is driven by the motivation to predict fluid interaction through the creation of mixing models for buoyancy- and shear-driven instabilities. This work combines experimental data and computational results to examine Rayleigh-Taylor and Kelvin-Helmholtz instabilities and to determine ways to decrease these instabilities' mixing. Previous experimental data was used to obtain appropriate initial conditions for the computational implicit large eddy simulation problem, which was then used to predict the effect of changing various parameters on the mixing width.

1.2 The Rayleigh-Taylor Instability

Buoyancy-driven instabilities occur when one fluid of density ρ_1 is accelerated into a second fluid of density ρ_2. This change in velocity can be caused by a natural acceleration such as gravity acting on a body or by a prescribed acceleration such as a device physically advancing the two fluids. For the Rayleigh-Taylor hydrodynamic instability in particular, the unsteadiness is caused by a heavier fluid being positioned above a lighter fluid relative to the acceleration such that $\nabla p \cdot \nabla \rho < 0$, where p is the pressure of the system (Rayleigh 1883; Taylor 1950). This instability evolves in three distinct steps: initial exponential growth, non-linear saturation, and multi-mode mixing (Sharp 1984). From linear stability theory, an initial sinusoidal perturbation of wavelength λ begins to grow exponentially; it is important to note that even in an unstable configuration some perturbation of the interface is necessary for a

hydrodynamic instability to begin to mix (Chandrasekhar 1961). The description of the instability using a linear stability scheme is only appropriate for small amplitudes (0.1λ to 0.5λ), after which point the disturbances become non-linear and saturate (Sharp 1984; Youngs 1984). This non-linear interaction creates structures that have come to be associated with Rayleigh-Taylor instabilities: fluid of lower density rising to a height "h_b" from the interface is termed a "bubble", whereas higher density fluid falling to a height of "h_s" from the interface is known as a "spike" (Kull 1991). These forms can arise either from the initial conditions or, if the initial perturbation is relatively small, from the non-linear interactions. As the bubbles and spikes continue to penetrate the fluid, secondary interactions known as Kelvin-Helmholtz instabilities appear along the edges of the aforementioned structures (Helmholtz 1868; Kelvin 1871). The observations described pertain to single mode initial condition disturbances. Because lower wavelengths saturate to non-linearity first, they are soon overtaken by longer wavelengths which are still growing exponentially. This occurrence results in multi-mode mixing, producing a number of length scales within the instability. These structures of assorted sizes then begin to interact through bubble competition and growth, wherein larger bubbles absorb smaller ones resulting in increases in size and velocity for the subsequent bubble (Sharp 1984). This process has been studied numerically (Freed *et al.* 1991; Bernstein & Book 1978; Sharp 1984), experimentally (Emmons, Chang, & Watson 1960; Dalziel, Linden, & Youngs 1999; Dimonte & Schneider 2000; Read 1984), and through simulations (Ristorcelli & Clark 2004;

Youngs 1984; Cook, Cabot, & Miller 2004; Kadau *et al.* 2010) to deduce a relationship for the late time heights of bubbles and spikes as

$$h_{b,s} = \alpha_{b,s} A_t g t^2 \tag{1.1}$$

where $\alpha_{b,s}$ is the growth parameter for the bubble or spike, respectively, $A_t \equiv (\rho_1-\rho_2)/(\rho_1+\rho_2)$ is the Atwood number for the system, g is the imposed acceleration, and t is time. For small Atwood numbers ($A_t < 0.2$), $\alpha = \alpha_b = \alpha_s$ and $h = h_b = h_s$, resulting in a self-similar growth of the instability. An image depicting the evolution of the Rayleigh-Taylor instability can be seen in Figure 1.

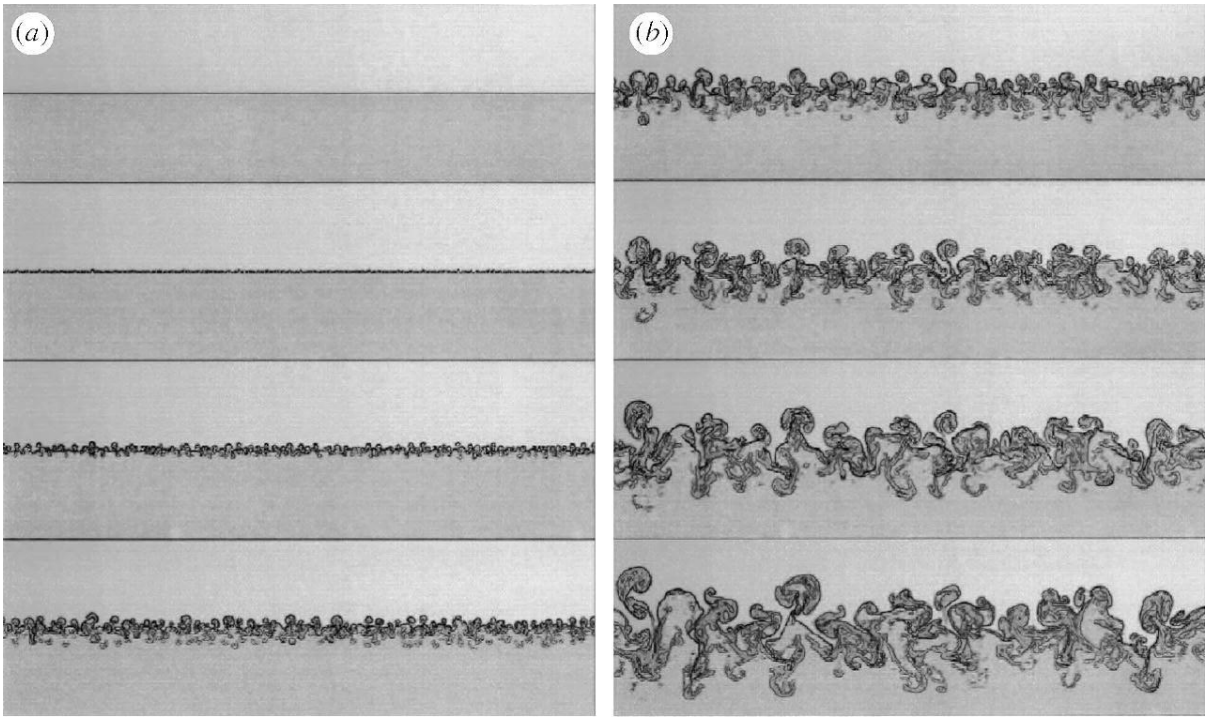

Figure 1.1. Rayleigh-Taylor instability simulation with $A_t = 0.67$ at times ((a) top to bottom) 0 τ, 4.6 τ, 9.2 τ, 13.8 τ and ((b) top to bottom) 18.4 τ, 22.95 τ, 27.5 τ, and 31.1 τ where τ is the exponential growth time of the most unstable mode (Kadau *et al.* 2010).

Rayleigh-Taylor instabilities can be seen throughout the universe in all scales of time and space. Among the largest in spectral scale are super nova remnants, in which Rayleigh-Taylor instabilities enhance the radial magnetic field and modify the geometry of the structure (Blondin & Ellison 2001; Fraschetti, Teyssier, Ballet, & Decourchelle 2010). One of the largest in temporal scales are oil trapping salt domes which develop over 30 million years from kilometers of dense earth compressing underground salt, causing it to flow upwards (Zaleski & Julien 1992). A smaller instance of spectral scale can be seen in droplet disintegration when exposed to a high velocity airstream. As the drag force decelerates the fluid, an unstable interface with a density gradient is created, thus forming the Rayleigh-Taylor instability (Bayvel & Orzechowski 1993; Baumgarten 2006). Among the smallest temporal and spectral scaled Rayleigh-Taylor interactions are those created during implosion of the ICF fuel capsule, a process which only lasts around 10 seconds. As mentioned previously, this instability prevents the formation of a heat concentration at the center of the fuel cell, thus inhibiting high-yield ICF from being obtained (Oron, Alon, & Shvarts 1998; Wilson *et al.* 2004). Despite the large range of applications for the Rayleigh-Taylor phenomenon, much is still left unknown about this buoyancy-driven instability.

1.3 The Kelvin-Helmholtz Instability

Shear-driven instabilities occur when one or more horizontally stratified fluids are streaming at a constant but different velocity for each fluid layer. For the Kelvin-Helmholtz instability in particular, a fluid of density ρ_1 moving with velocity U_1 is positioned above either the same fluid or a second fluid of density $\rho_2 > \rho_1$ which is

moving with velocity U_2 (Helmholtz 1868; Kelvin 1871). Since the density of the lower fluid is greater than or equal to that of the top fluid, $\nabla p \cdot \nabla \rho > 0$, where p is the pressure of the system, and no Rayleigh-Taylor instability is present. The two velocities can be modeled as equal and opposite vectors moving along the interface with a speed of $(U_1-U_2)/2$. This setup results in the generation of a vorticity (equation (1.2)) which is positive when the relative velocity is greater than zero and negative if it is less than zero.

$$\vec{\omega} = \frac{\nabla \rho \text{ x } \nabla \text{p}}{\rho^2} \tag{1.2}$$

A positive vorticity causes fluid to be swept away from that location while a negative one causes fluid to be pulled towards that point (Batchelor 1967). This process results in fluid-accumulating sites which rotate clockwise or counterclockwise, depending on which stream has the greater velocity, thus amplifying the interface displacement (Drazin 2002). As this instability continues to develop, exponential growth of the interface presents, followed by multi-scaled turbulent motions; the rollups then begin to overlap and merge into a single disturbance before diffusing out (Woods & Wiley 1972). A schematic depicting the growth of the Kelvin-Helmholtz instability can be seen in Figure 1.2.

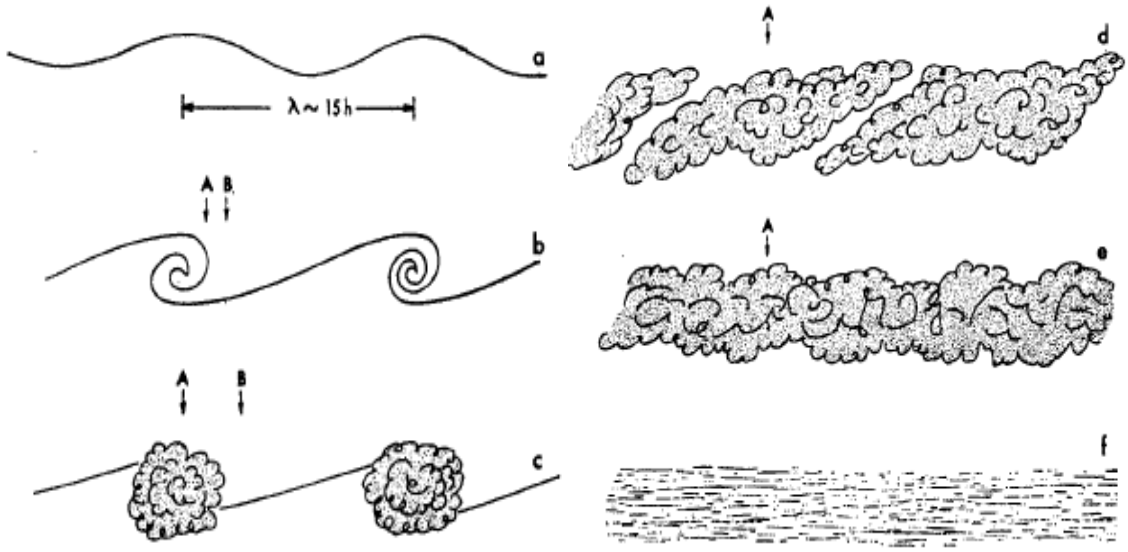

Figure 1.2. Kelvin-Helmholtz instability schematic developing with time. a: initial interface disturbance, b: interface rolls up due to applied shear, c: multi-scaled turbulence arises in structure, d: turbulence spreads throughout interface, e: turbulent rollups merge into a single disturbance, f: molecular diffusion removes high wavenumber components (Woods & Wiley 1972).

Kelvin-Helmholtz instabilities can be seen in all length scales throughout the universe. One of the largest scales occurs at the boundary between the sun's surface and its corona, a plasma atmosphere protruding millions of kilometers from the star's surface (Ofman & Thompson 2011). As the eruption transpires, a velocity shear is created between the two planes, thus creating the instability. On a slightly smaller scale, the magnetopause between a planet's magnetosphere and plasma is highly inclined to shear-driven instabilities. The specific location of this structure is determined by the opposing planetary magnetic field pressure and the dynamic solar wind pressure (Amerstorfer *et al.* 2007). As the solar wind fluctuates, the magnetopause accordingly changes, creating a perturbation which combined with the solar wind causes the instability to develop

(Walker 1981). One of the most common instances of Kelvin-Helmholtz instability on Earth is gravity waves, such as in clouds or on the ocean, caused by wind flowing over a denser fluid (Miles 1957). This variety can extend in size anywhere from a few kilometers (such as clouds or large waves) down to a few millimeters for water ripples. One of the smallest instances of Kelvin-Helmholtz instabilities results from Rayleigh-Taylor instabilities in ICF. As the bubbles and spikes rise and fall in the fluid, respectively, a shear layer between the two structures is created. This action results in the widening of the two entities and gives rise to the mushroom structure that is associated with non-linear Rayleigh-Taylor instabilities (Emery *et. al* 1982; Sharp 1984). Much like the Rayleigh-Taylor instability, much is still left to be discovered with this shear-driven instability.

1.4 Previous Work

Hydrodynamic instabilities have been a subject of research for the past few centuries because of their application to both everyday experiences and state-of-the-art innovations. Some examples from the former category include flow in pipes (Orszag 1971; Wang & Rusak 1996; Hof *et al.* 2004), combustion (Sivashinsky 1977; Sivashinsky & Clavin 1987; Gutman & Sivashinsky 1990), solute transfer (Sternling & Scriven 1959), and evaporation (Palmer 1976). As for the latter, instabilities play a role in ink jet technology (Moseler & Landman 2000; Duineveld 2003), capillary liquid bridges used for crystal growth and material science (Kuhlmann & Rath 1993), ICF (Tabak, Munro, & Lindl 1990; Remington *et al.* 1993; Azechi *et al.* 1997), and astrophysics (Perri & Cameron 1974; Lai, Rasio, & Shapiro 1993; Ji *et al.* 2006). The

previous investigations into hydrodynamic instabilities can be split into three categories: experimental, numerical, and computational modeling.

1.4.1 Experimental studies of hydrodynamic instabilities

The diversity and complexity of buoyancy-driven instabilities has evolved in time as acceleration and imaging mechanisms have continued to develop. One of the first experimental investigations of Rayleigh-Taylor instability was conducted by Lewis (1950) using compressed air to create accelerations up to 75 times that of gravity and shadow photography to capture the images for later analysis. He then examined the photographs to evaluate the mixing width of the instability for different degrees of acceleration. From his results, Lewis was able to conclude that the instability initiates as exponential growth according to linear stability theory, followed by a transitional period in which the amplitude increases and the surface disturbance accordingly changes, until finally a uniform velocity is reached.

The development of the rocket rig in 1983 advanced the world of buoyancy-driven experiments as it is less expensive in cost and manufacturing time over compressed air, and it allows for near-constant acceleration over a long distance (Read 1984). The apparatus consists of a tank initially arranged in a stable configuration, with a fluid of lower density positioned above one with higher density. On the frame are two rocket motors which utilize solid fuel to propel the tank downward faster than the acceleration of gravity, thus causing $\nabla p \cdot \nabla \rho$ to be less than zero, creating the instability. Photographs taken at 200 frames per second were used along with a distance scale on the rocket rig frame to evaluate the degree of fluid mixing.

From this new technology, multiple experiments with various fluid combinations became available (Smeeton & Youngs 1987). A three-fluid experiment with the same Atwood number between the top and middle as well as middle and bottom fluids was conducted. Results were shown to compare well with previous experiments and allowed for the creation of equations to compare the mixing widths of the top- and bottom-most fluids. A tilted rig experiment was run at two different angles to evaluate and validate two dimensional dominant flows, with an increasing angle relating to a greater degree of two dimensional effects. Comparing the resulting mixing width to an experiment with identical conditions minus the tilt, the values match at early times, but the former eventually levels out as the spike growth slows down. This trend has been seen in previous experiments, but not at such a prominent drop off. Experiments under constant acceleration, acceleration then coast, and acceleration then deceleration were evaluated to determine the change in the volume fraction with time, which was expected to evolve primarily in a linear fashion. The growth rate was linear when acceleration was constant, leveled off when coasting and decreased when the rig was decelerated. Experiments with miscible fluids demonstrated significant molecular mixing, and the use of compressed SF_6 allowed for trials with Atwood numbers up to 0.94. For all cases, the growth rate was consistently around 0.06.

The level of mixing does not purely rest on the Atwood number; the initial condition of the interface between the two fluids has a large effect. If the interface is perfectly flat, the instability will not proceed to blend as neither fluid is able to break the boundary. Further, two perturbations which deviate slightly from one another can have

instabilities which evolve in vastly different ways. As such, initial conditions have been the subject of focus as of late. Though it is difficult to determine the initial perturbations in ICF, experiments can be created with prescribed conditions, and the resulting late time behavior can be studied. One such example was carried out by White *et al.* using magnetorheological fluid positioned over a fluid of lower density (2010). A mold was created in the shape of a sine wave with amplitude of 0.16 cm and wavelength of 2.12 cm, upon which water was poured and allowed to freeze. The mold was then removed, magnetorheological was placed on top of the ice and immobilized with magnets, and the ice was allowed to melt. This left the system with an unstable configuration with Atwood number of 0.46 once the magnets were removed. After the magnetorheological fluid is immobilized, the water can be drained to give an air interface with Atwood number of almost one. Optical and x-ray visualization techniques are utilized to capture the instability advancement. Results show asymmetry in the saturated growth rates, as is the case with several other papers, giving validity to the findings. The capability of the setup to obtain repeatable and precise initial conditions through the creation of molds provides a great step in determining the relationship between initial perturbations and late term growth of Rayleigh-Taylor instabilities.

Kelvin-Helmholtz instabilities, which present in nature independently, also occur at the boundary layer of Rayleigh-Taylor instabilities. With the focus of buoyancy-driven instabilities increasing, shear-driven instabilities have consequently gathered more attention. Experiments have been conducted to study this phenomenon and compare it to those occurring in nature (De Silva *et al.* 1996). In this example, a

rectangular box with its long axis in the vertical direction is filled with two fluids of different densities in a stable arrangement. The box is then tilted by a certain angle, forcing the fluid to stretch and produce the instability. Imaging was accomplished using recorded video as well as photographs near the center of the tank to avoid wall effects. Through dye selection and laser induced fluorescence, the degree of mixing throughout the rollup can be observed and is shown to be greatest at the center. Eventually, the center of the rollup breaks down to a spot of turbulence which ultimately spreads throughout the structure.

One of the key players in Kelvin-Helmholtz instability is vorticity, which acts to create the rollups typically associated with the instability. However, the vortex sheet that forms at the interface of the two fluids is not stable, thus producing outcomes contrary to those predicted in Kelvin's initial theory. By studying fluids in which vorticity is almost zero, namely supercritical flows, the theory and physical experiments can be better compared (Blaauwgeers *et al.* 2002). Using two phases of supercritical helium, the former with solid-body like rotation and the latter with vortex-free status, the rotational velocity can be increased to the point at which instability is reached for observation. The arrangement, which is at magnetically stabilized, initially experiences rotation in the upper fluid of solid-body rotation. Once the degree of revolution causes the upper fluid to extend into the lower fluid free of vortexes, the arrangement becomes unstable and the instability begins to develop. The result is the transmission of vorticity across the interface, thus creating perturbations in the interface which further pull the vortex lines through the boundary of the two fluids. To further study the effect of

vorticity in Kelvin-Helmholtz instability, vorticity probes have been used to quantify the effect this occurrence has in the flow field (Horton *et al.* 2005). Shear is created using magnetic and electric fields, and the probe is used to collect vorticity data as the instability develops. From the experiment, it was determined that the vorticity exhibits large values for most of the run, and also changes signs in multiple locations throughout the interface. This asymmetric quality is at the core of Kelvin-Helmholtz theory.

With the construction of the Texas A&M University water channel device in 1994, and later the gas channel in 2006, statistically steady hydrodynamic instabilities with large data collection times could be studied (Snider & Andrews 1994; Banerjee & Andrews 2006). The channel allows for an unstable configuration initially separated by a splitter plate to begin mixing once it enters the test section. Since the channel is convective in nature, the flow is steady in time but not in space as the instability continues to develop as the fluid moves downstream. The density of the bottom stream can be decreased by heating it for the water channel or injecting helium into it for the gas channel, thus creating an unstable arrangement. Proceeding in this manner provides Atwood numbers ranging from 0.00034 to 0.0014 for the former and 0.03 to 0.75 for the latter. Fog is added to the bottom stream for visualization and for aid in determining the volume fractions. Using a wedge calibration system, with the bottom stream having the least intensity and the top stream the most, the mixture fraction and growth rates throughout the flow field can be determined. Both channels have the capability to produce a shear between the two flow streams through increasing or decreasing the exit velocity of one of the fluids. In doing so, Kelvin-Helmholtz instabilities are created, and

if coupled with the density difference mentioned above Kelvin-Helmholtz Rayleigh-Taylor combined instabilities present.

1.4.2 Simulation studies of hydrodynamic instabilities

With the advent and development of computational technology, the study of hydrodynamic instabilities through simulation and modeling has rapidly progressed. David Youngs, a pioneer in the field of buoyancy-driven instabilities, utilized this new equipment to model the instability and compared it to the works of his colleague Read discussed earlier (Youngs 1984). At the time, the computational resources could only model up to two-dimensions, offering understanding of the large scale structures and behaviors but preventing the study of small eddies which undergo viscosity dampening. The multi-mode simulations, which are more complex and require more computational resources, closer replicate physical experiments. Further, with multi-mode perturbations the mixing rate soon becomes insensitive to the initial conditions and follows a simple pattern of progression. In 1995, Andrews employed the Van Leer method to compute the convective fluxes in two-phase flows (Andrews 1995). This method uses meshes to approximate the initial pressure distribution and ensure that it is conserved. The distribution is then convected, the mesh is remapped, and weights on the functions are applied based on least squares fitting (Van Leer 1977). Since the scheme prevents erroneous extremes and operates under higher order accuracy, the physical actuality is maintained. This attribute is especially important when there are multiple fluids in the simulation, as the fraction of fluids must always be between zero and unity. This code was then further modified to determine the effect of initial conditions on mixing

(Banerjee & Andrews 2009). Three types of perturbations were utilized in the study (spectral bandwidth, spectral shape, and discrete banded spectra) to evaluate their effect on growth rates. It was determined that when the initial perturbation contained more energy in the higher wavenumbers the instability grew faster. Conversely, when the initial condition had more energy in the low wavenumbers the instability proceeded slowly. Further, as the longest wavelength in the system was increased, the bubble growth rate directly increased as well. These results, along with other findings, authenticates that the total growth of the system relies heavily on the initial perturbations of the fluid interface.

Taylor, a forerunner in the field of buoyancy-driven instabilities, was also investigating the effect of shear on different layers of stably arranged fluids (Taylor 1931). He investigated the effect varying the density in the different layers had on the behavior and stability of the total system. In his work, he solved numerous equations for cases with varying degrees of density, velocity, and phases; he then reportd the necessary conditions to produce unstable configurations for all situations considered. One of the first simulations of shear-driven instabilities was conducted to gain a better understanding of why the characteristic rollup structures occur in nature. The research team used a finite difference technique to solve the Boussinesq equations and modeled the results on a rectangular two-dimensional grid (Patnaik *et al.* 1976). The findings support the linear stability theory at the low amplitude, early time stage of the instability, as well as the combination of rollups into subsequent structures. The team notes that this incorporation depends on the phase shift between the rollups and the relative rate of

growth, among other factors, but does not have the capabilities to explore the modal interactions in depth. To develop a deeper understanding of the instability, it must be modeled in three dimensions to capture secondary disturbances that arise. Scinocca undertook this task to investigate how mass and momentum mix throughout the roll up process (Scinocca 1995). Through this technique, he was able to gain some understanding of the development of secondary structures, for instance that the instability begins in the outermost layer of the rollup, then transitions inward as time progresses. Further, as the Richardson number, ratio of Rayleigh-Taylor to Kelvin-Helmholtz effects, decreases the flow tends toward producing highly defined vortex structures. This tendency can be explained through the absorption of rollups until only the strongest, most prominent forms remain. The system's behavior was concluded to be highly dependent on the strength of the fluid stratification shear; the mixing efficiency as well as mass and momentum flux increased as the shear between the fluid layers was increased. This trend can be contributed to a higher growth rate of the instability with rising shear, thus producing a greater degree of instability and an increased likelihood of fluid mixing.

Of utmost interest as of late is modeling how buoyancy- and shear-driven instabilities interact when combined in the same system. In 1981, Emery *et al.* investigated the effect of laser ablation on a flat interface and the resulting hydrodynamic instabilities that arise from the process (Emery *et al.* 1982). This task was carried out by utilizing a two-dimensional Cartesian based code with variable grid spacing. As the code progresses in time, it transitions to the nonlinear regime and

depicts the characteristic bubble and spike Rayleigh-Taylor structures observed in physical experiments. As these entities continue to grow, the relative shear produces secondary Kelvin-Helmholtz instabilities at their interface, causing their penetration to slow as their width increases. Through analysis of velocity, density, and temperature plots, the effect of the two instabilities and how they interact can be investigated in depth. The results demonstrate the stabilizing effect the shear has on the bubble and spike structures and suggest this may be the key to stagnating the fluid mixing before the shell is completely fragmented. An alternative way to investigate the combined effect of buoyancy- and shear-driven instabilities is in Z-pinch implosions. As the magnetic field compresses the plasma, a Rayleigh-Taylor instability is created in the system. In an attempt to mitigate this effect, Shumlak and Roderick investigated adding a parallel shear to the arrangement in order to stabilize the reaction, much the way the Kelvin-Helmholtz instability slowed the bubble and spike growth discussed earlier (Shumlak & Roderick 1998). Using a magnetohydrodynamic model, a Z-pinch with an unstable density arrangement is configured, and then a parallel velocity is imposed on the overall system. The velocity given to the Z-pinch is increased to higher and higher values until the amplitude of the bubbles and spikes is shown to decrease dramatically. The addition of the Kelvin-Helmholtz instability is thus shown to mitigate the effect of the Rayleigh-Taylor instability, offering a solution to preventing this unwanted side effect and confirming previous simulations with similar provisions. An alternative way to contain both instabilities in a scheme is to have the two interacting perpendicular to one another. In this scenario, the theory predicts an increased growth rate over a pure Rayleigh-

Taylor interaction. However, Olson and his collaborators strove to prove this concept to be untrue and that the growth rate actually decreased initially with shear before later expanding as the level of shear increased (Olson *et al.* 2011). In order to accomplish this task, they utilized a large eddy simulation and ran six different cases with increasing shear. Through the analysis of growth rates, mixing rates, mixing efficiency, and density contours, the effect of different levels of shear can be evaluated throughout the stages of the instability. Analysis of the results demonstrated an initial decrease in mixing rate during the nonlinear growth phase when the shear was low. This trend can be attributed to the change in shape from mushrooms to rollups with the addition of shear. As the shear increases, the energy in the system increases and allows the mixing width to thus grow further than a purely buoyancy-driven system. These findings provide the hope that the effects of Rayleigh-Taylor instability can be limited with the addition of a controlled Kelvin-Helmholtz instability to the system.

1.5 Research Objectives

The objective of this research expedition is to investigate the effect of initial conditions on the level of mixing in the hydrodynamic instability. This mission was undertaken in order to solve the following quandaries:

1. What role does the Atwood number play in fluid amalgamation?
2. What effect does the initial condition of the fluid interface have on mixing? In particular, how does mixing width and level of molecular mixing vary as the number of initial modes is changed?
3. What effect does initial velocity fluctuation have on Kelvin-Helmholtz mixing?

4. What effect does shear have on the growth rate, mixing width, and Richardson number of the system? What is the transitional Richardson number at different shears, and is there any correlation for this characteristic?
5. Using the results obtained from the previous items, is there a potential way to control the level of fluid mixing through the selection of specific initial conditions?

These questions have been resolved through the combined use of an implicit large eddy simulation computational code under active development at Los Alamos National Laboratory and Texas A&M University. Experimental data obtained from the Texas A&M University gas channel have been utilized for initial condition selection as well as comparison to the computational results. The ways in which the above queries were investigated are as follows:

1. Run cases with Atwood numbers ranging from very low (0.032) to high (0.6), and compare mixing width and molecular mixing parameter θ (when applicable).
2. Run cases with identical settings apart from the initial boundary condition. Assign one variety with a single mode initial boundary perturbation and another with initial conditions based upon the density power spectrum taken just after the splitter plate in the Texas A&M University gas channel (Akula *et al.* 2012). Compare the mixing width and molecular mixing.
3. Run cases with varying levels of vertical velocity fluctuations based on hot wire anemometry data. Compare with experimental data for mixing width and height gradient.

4. Run cases with identical settings apart from the relative shear in the two fluid layers. Compare the growth parameter, mixing width, molecular mixing, and the Richardson number. Analyze the derivative of the mixing width to determine how it changes with regard to the Richardson number.
5. Analyze the results obtained from the above methods and investigate the techniques which result in the smallest mixing width, molecular mixing, and growth parameter.

1.6 Outline of Thesis

First, the implicit large eddy simulation computational code under active development at Los Alamos National Laboratory and Texas A&M University was modified to replicate buoyancy- and shear-driven instabilities. Using this updated code, three cases based on published experimental Rayleigh-Taylor data were used to analyze different Atwood number problems with values of 0.032, 0.46, and 0.6. Comparisons of these results were utilized to authenticate the code and to evaluate how the degree of fluid mixing changes as the density difference between the two layers increases. Next, the 0.032 Atwood number case was investigated in depth with two different interface perturbations, four different velocity fluctuations, and six different amounts of shear. The relative shear between the fluids was 0m/s (pure Rayleigh-Taylor case), 0.2 m/s, 0.35 m/s, 0.5 m/s, 0.65 m/s, and 0.8 m/s. A pure Kelvin-Helmholtz case with relative shear of 0.8 m/s was also studied and contrasted against the six previously mentioned cases. Differences in mixing widths, molecular mixing, growth parameter, and Richardson number for the initial conditions were obtained and utilized to investigate relationships with fluid

mixing. In addition, the height gradient of the mixing width was utilized to determine the relative levels of Rayleigh-Taylor and Kelvin-Helmholtz effects and at what transitional Richardson number these come into play.

2. CODE VALIDATION AND ANALYSIS OF ATWOOD NUMBER EFFECT

2.1 Overview of Goals and Methodology

The first step taken to complete the tasks laid out above was to transform the provided computational code into a vehicle to model the desired problems at hand. Upon converting the code into a more versatile version, the ability of the program to accurately model hydrodynamic instabilities needed to be verified. This duty was accomplished through comparison of the code to physical experiments as well as to proven theory. Upon gaining confidence in the capabilities of the code, three different Atwood number cases were considered in order to determine the role density plays on fluid mixing. Relationships of the mixing width and molecular mixing of the three instances to physical experiments as well as to each other were investigated.

The mixing width of the system was calculated as the height difference between the locations of bottom stream fluid volume fraction contours at 0.05 and 0.95. The volume fractions are calculated as

$$f_1 = \frac{\rho - \rho_2}{\rho_1 - \rho_2}, \quad f_1 + f_2 = 1 \qquad (2.1, 2.2)$$

where f_1 is the top fluid's volume fraction, f_2 is the bottom fluid's volume fraction, ρ is the density value at the current point, ρ_1 is the density of the top fluid, and ρ_2 is the density of the bottom fluid. The amount of molecular mixing in the fluids is found by taking into account both the effect of mixing due to molecular diffusion and the condition that would result if both fluids were immiscible and thus no molecular mixing occurred. The former can be seen in equation (2.3) where T is the total system time, $\bar{\rho}$ is the average density, and $\Delta\rho$ is the density difference; the latter is shown in equation

(2.4). Combining these two equations results in the equality for the molecular mix fraction θ measured at the centerline (2.5).

$$B_0 = \lim_{T\to\infty} \frac{1}{T} \int_0^T (\rho - \bar{\rho})^2 dt / \Delta\rho^2 \tag{2.3}$$

$$B_2 = f_1(1 - f_1) \tag{2.4}$$

$$\theta = 1 - \frac{B_0}{B_2} \tag{2.5}$$

Inside the mixing width, θ equals zero if the two fluids are immiscible and equals one if the two fluids are completely mixed molecularly. At the centerline, B_2 tends toward its maximum value (0.25), meaning both fluids are equally present. This parameter becomes smaller the further it gets from the centerline, with its minimum value occurring at the edge of the mixture. B_0 is equal to zero when either the fluids are completely mixed or when only one fluid is present.

2.2 Code Description

The initial code (called RTI3D) provided from Los Alamos National Laboratory is a research program which is currently under active development jointly at Los Alamos and Texas A&M University. This implicit large-eddy simulation framework is commonly used to model fluid instabilities (Banerjee & Andrews 2009). RTI3D utilizes a finite volume technique with third order Van-Leer equations for flux calculations and a multi-grid solution method to resolve pressure terms. This code solves three-dimensional incompressible Euler equations, although the option of applying Navier-Stokes equations is also available. The implicit large-eddy simulation scheme exploits numerical dissipation to model turbulent diffusion. This technique serves to dissipate

small scales in a manner similar to physical viscosity. The program is capable of modeling cyclic boundary conditions in both the x and y planar directions, while the z boundary is held under a free-slip condition (see Figure 2.1). The initial framework was set up to model a tilted rig instability, a Rayleigh-Taylor density instability where the interface between the two fluids is slanted.

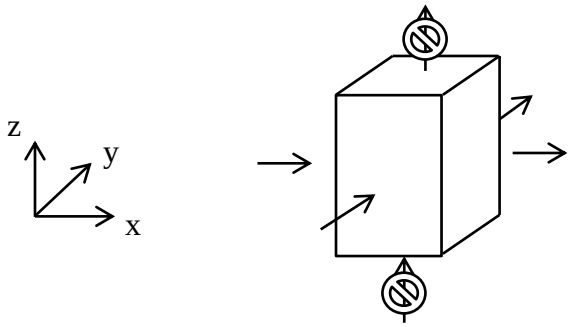

Figure 2.1. Depiction of computational box with cyclic x and y and free-slip z boundaries.

The incompressible Eulerian governing equations can be seen in volume conservation (equation (2.6)), scalar transport (equation (2.7)), and momentum balance (equation (2.8)), where $\vec{u}$ is the three component velocity vector, f is a scalar, t is time, ρ is density, P is pressure, and $\vec{g}$ is the three component gravity vector. This combination results in five equations with six unknowns; the sixth equation comes from the assignment of the scalar to the mix fraction as described in (2.1).

$$\nabla \cdot \vec{u} = 0 \tag{2.6}$$

$$\frac{Df}{Dt} = 0 \tag{2.7}$$

$$\frac{D(\rho\vec{u})}{Dt} = -\nabla P + \rho\vec{g} \tag{2.8}$$

The code works to first solve the advection terms then update the Lagrangian source terms; this is done using a fractional time step technique. For the first segment, the three dimensional transport is split into steps for each component. This technique simplifies the problem to a series of one-dimensional updates, resulting in higher order calculations of cell fluxes with the Van Leer method. Starting with the x-component of the scalar transport, the advection is given by

$$f_P^* = f_P^n + \Delta y \Delta z \Delta t (u_e f_e - u_w f_w) \tag{2.9}$$

where p is the center of the control volume, e and w is the east and west face, respectively, n is the current time step, and * is the intermediate time step. The velocity values at the faces are known, and the scalar quantities at the faces can be found from a second order approximation using Van Leer limiting so as to avoid non-physical oscillation. This equality and subsequent definition of terms can be seen below. Because the gradient of the cell profile (D) is computed with a central difference method, the scheme is second order. Following this technique, the other components of the scalar transport can be found, and similar advection steps can be performed for the momentum.

$$f_e = f_{upwind} + \text{sign}(\varepsilon_e)\frac{(1-\varepsilon_e)}{2}\Delta x D_e \tag{2.10}$$

$$\varepsilon_e = \Delta t u_e / \Delta x \tag{2.11}$$

$$D_e = S \min\left\{|D|, \frac{2|\Delta w|}{\Delta x}, \frac{2|\Delta e|}{\Delta x}\right\} \tag{2.12}$$

$$\Delta w = f_P^n - f_W^n \tag{2.13}$$

$$\Delta e = f_E^n - f_P^n \tag{2.14}$$

$$S = \begin{cases} 1 & \text{if } \Delta e \text{ and } \Delta w > 0 \\ -1 & \text{if } \Delta e \text{ and } \Delta w < 0 \\ 0 & \text{otherwise} \end{cases} \tag{2.15}$$

$$D = \frac{\Delta e + \Delta w}{2\Delta x} \tag{2.16}$$

The second fraction of the time step is used to update the Lagrangian momentum source term. The equation for the w component is

$$w_n^* = w_n^{n+1/2} + \frac{\Delta t}{\rho_t \Delta y}\left(P_p^n - P_T^n\right) + g_z \tag{2.17}$$

where n+1/2 is the intermediate value from the previous advection calculation and * is the intermediate value which may or may not satisfy continuity. The velocity and pressure corrections, respectively, are

$$u_{i,e}^{n+1} = u_{i,e}^* + \Delta u_{i,e} \tag{2.18}$$

$$P_p^{n+1} = P_p^n + \Delta P_p \tag{2.19}$$

Substituting these equations into the volume conservation relation and removing the momentum equation results in the Poisson equation for pressure corrections set equal to the divergence of the intermediate velocity values which do not necessarily satisfy continuity:

$$a_P \Delta P_p + a_E \Delta P_E + a_W \Delta P_W + a_N \Delta P_N + a_S \Delta P_S = -\mathrm{Div} \tag{2.20}$$

This equation is solved with a multi-grid method then the resulting pressure corrections are used along with the SIMPLE algorithm to update the velocities and pressures while ensuring momentum and velocity is conserved.

2.3 Code Modification

Upon receiving of the RTI3D code described above, a number of modifications were implemented in order to model the desired instability. First, the slanted interface characteristic of the tilted rig was removed. In its place, the code was set up with a velocity perturbation in the form of a sine wave. A single mode had the form of:

$$M_1 = \text{sgn} * \sin(k * x) * e^{-k*|z|}/k \tag{2.21}$$

where sgn is positive or negative depending on if the location is on top or bottom of the interface, respectively, k is equal to the wavenumber, and z is the current height location. Multiple perturbations with a similar form can be added to the code to provide a multi-mode initial interface condition. The next step in the process to model the fluid instabilities was to allow for shear in the system. The code was initially set to input one velocity value, which was then distributed across the height of the modeled instability. The program was then modified to allow for two separate velocity values, one for each stream, which were transitioned near the interface in order to prevent discontinuities where the fluids met. With this arrangement, the fluid was assembled with an actual reference frame, in which a setup with top fluid moving at 1m/s and bottom fluid moving with bottom velocity of 0.2 m/s is modeled directly with those velocities. An alternative technique is to utilize an inertial reference frame, in which the average velocity is subtracted from each value, resulting in equal and opposite values, ±0.4 m/s in this instance. Due to convection inconsistencies within the code, it was determined that the inertial reference frame provided the most realistic results. The initial interface perturbation was thus set up with this arrangement for all cases. Additional code

segments were created to capture various data points for future modeling, including bubble and spike heights, molecular mixing, Richardson number, velocity values, etc. The final modification to the code was done in the input file where the density and velocity values were set to match those in the physical experiments.

2.4 Comparison to University of Wisconsin-Madison Experiment, Atwood Number 0.46

The first goal with the newly updated code segments was to model published physical experiments in order to validate that all changes were carried out correctly and result in physiologically accurate outcomes. The first paper chosen was White *et al.*'s work on a Rayleigh-Taylor instability with sharply defined initial interface perturbation (White *et al.* 2010).

2.4.1 Description of physical experiment

The two fluids used in the experiment were magnetorheological fluid, which has a density of 2735 kg/m^3, and water with a density of 1000 kg/m^3. The instability was created using a metal sheet formed in the shape of a sine wave with amplitude 0.08 cm and wavelength of 2.12 cm. The sheet was placed in the middle of the experimental container, and water was pumped into the lower half and frozen. The sheet was then removed and magnetorheological fluid was added on top of the ice and held in place with two magnets. The ice was then allowed to completely melt and the water to return to room temperature, at which point the magnets were retracted and the two fluids were allowed to interact. The resulting images from this experiment can be seen in Figure 2.2.

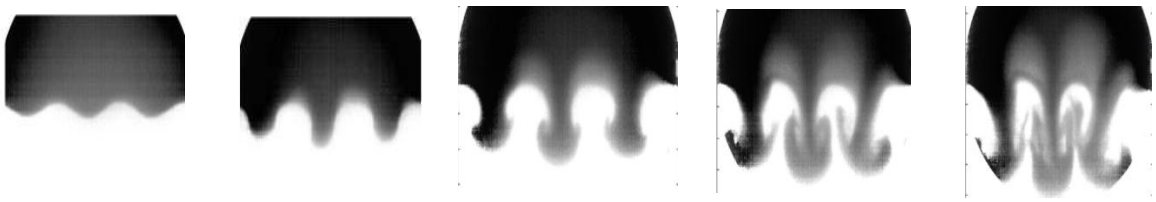

Figure 2.2. Images taken from experimental run by White *et al.* using magnetorheological fluid over water. From left to right, time after magnet retraction is: 0 ms, 52 ms, 116 ms, 152 ms, and 176 ms.

Optical and x-ray visualization techniques are utilized to capture the instability advancement. Results show the characteristic mushroom structures as well as asymmetry in the saturated growth rates. Through analysis of captured images, the mixing width and terminal velocity can be measured. Further, the results can be used to calculate the Froude number, a ratio of interita to gravitational forces which illustrates the resistance of an object's motion through water. The capability of the setup to obtain repeatable and precise initial conditions through the creation of molds provides a great step in determining the relationship between initial perturbations and late term growth of Rayleigh-Taylor instabilities.

2.4.2 Description of problem setup

In order to recreate this experiment computationally, a box with dimensions 7.6 cm x 1.27 cm x 20.3 cm was created with grid spacing of 64 x 16 x 256 to give a resolution of 1.188 mm x 0.794 mm x 0.793 mm in the x, y, and z directions, respectively. All grid spacings subsequent resolutions were determined based on the resolution study conducted by Banerjee and Andrews (Banerjee & Andrews 2009). The top fluid was given a density of 2735 kg/m^3 and a velocity of 0m/s while the bottom fluid was set to

density of 1000 kg/m^3 and velocity of 0 m/s. The program was set to run for a physical time of 168 ms with 180000 time steps, which took 30 minutes to compute, and was given the same perturbation as described above, resulting in a single mode in the form of

$$M_1 = \text{sgn} * \text{amp} * \sin(k * x) * e^{-k*|z|} \quad (2.22)$$

where amp=0.08 cm and k = $2\pi/\lambda = 2\pi/2.12$ cm. The x and y planar boundaries were set to be non-cyclic as the physical and computational dimensions matched.

2.4.3 Results from computational code

The mushroom structures characteristic of the Rayleigh-Taylor instability can be seen in the computational output (Figure 2.3) and match those in the images by White *et al.* Towards the end of the run, the mushrooms begin to tilt inward in both the experimental and computational cases, which together with the former give much validity to the code operating precisely with the new modifications. The only visible difference between the two cases is in the time it takes each one to reach the respective stages, with the computational code unraveling much faster than the physical experiment. This quality can be attributed to the residual magnetic impact in the magnetorheological fluid. Unlike in theory where when the magnets are retracted the fluids begin to mix instantaneously, in reality there is a residual magnetic force which is felt by the fluid, thus delaying the mixing in the system.

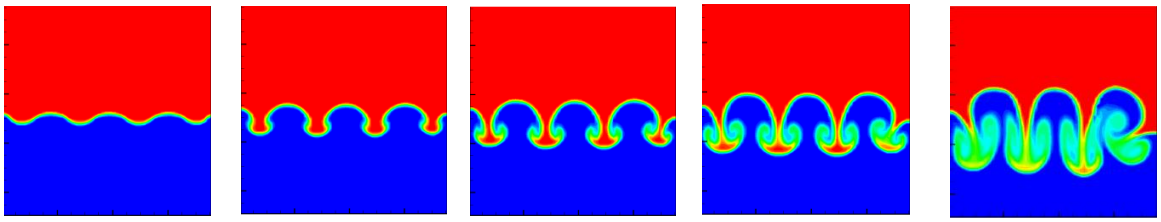

Figure 2.3. Images taken from computational run based on data from White *et al*. using magnetorheological fluid over water. From left to right, time after start of fluid interaction is: 6.65 ms, 21.6 ms, 40 ms, 60 ms, and 98 ms.

To further compare the two cases, the bubble and spike heights can be plotted against a normalized time t/t′ (Figure 2.4) where t′ is shown in equation (2.23). The bubbles and spikes have grown farther in the computational case due to the lack of residual magnetic effects described above. The above instances provide confidence to the ability of the code to model Rayleigh-Taylor experiments successfully.

$$t' = \sqrt{\frac{\lambda}{A_t g}} \tag{2.23}$$

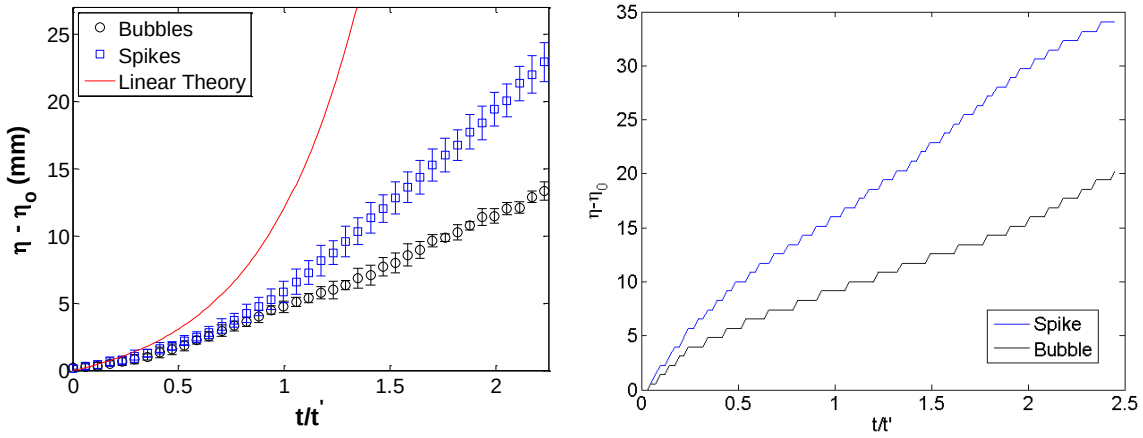

Figure 2.4. Depiction of bubble and spike amplitude height (η) versus normalized time. Left: experimental data, right: computational data.

The computational method offers a number of benefits and detriments over the physical experiment. For the former, the computation is able to evaluate up to a further time since the code is not limited by an imaging window (see Figure 2.5). As for the latter, the inability to know the exact initial conditions of the experiment hinder the code, as can be seen in the convex appearance of the amplitude heights at early time (2.4, right). The difference from the specifically set conditions in the experiment could be due to imperfections created when removing the mold or melting the ice and require further evaluation to perfect.

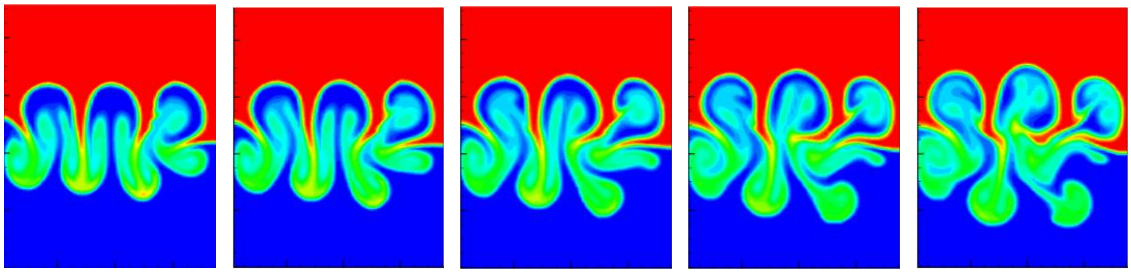

Figure 2.5. Late time images taken from computational run based on data from White *et al*. using magnetorheological fluid over water. From left to right, time after start of fluid interaction is: 114.2 ms, 127.7 ms, 141.1 ms, 154.6 ms, and 168 ms.

2.5 Comparison to Texas A&M University Experiment, Atwood Number 0.6

With the ability to model Rayleigh-Taylor instabilities proven, the next step was to increase the Atwood number to test the codes limitations. The paper chosen for this task was Banerjee and Andrews work in a statistically steady gas channel (Banerjee *et al.* 2010).

2.5.1 Description of physical experiment

The remaining experiments presented in this paper were carried out at the Texas A&M University gas channel mentioned earlier in the previous works section. Air enters the channel, which is split into two sections by a splitter plate, and flows through numerous meshes to ensure the flow is straightened (Figure 2.6). Upon exiting the meshes, the two fluids are allowed to mix and images are captured for future data analysis. Helium can be added to the bottom section as it enters the channel to create a density instability, or the flow can be altered to create a velocity difference between the two streams. The dimensions of the test section are 2 m x 0.6 m x 1.2 m.

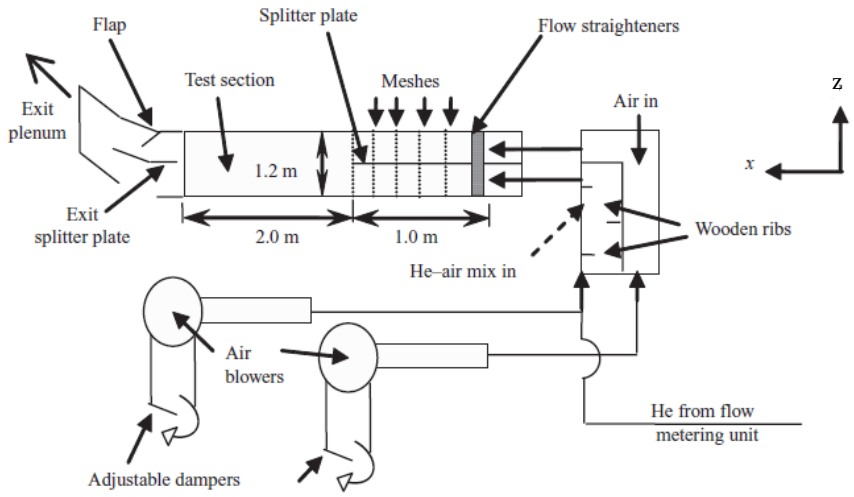

Figure 2.6. Schematic of Texas A&M University gas channel, side view.

The density of air in the experiment, and thus the density of the top fluid, is 1.14 kg/m^3. In order to obtain an Atwood number of 0.6, helium needed to be added to the

bottom stream until it reached a density of 0.285 kg/m^3. Unlike in White *et al.*'s experiment, the initial interface is not sharp and well defined. A picture of the run can be seen in Figure 2.7 while an image of the mixing width at two different locations is shown in Figure 2.8.

Figure 2.7. Image of test section from gas channel with Atwood number 0.6.

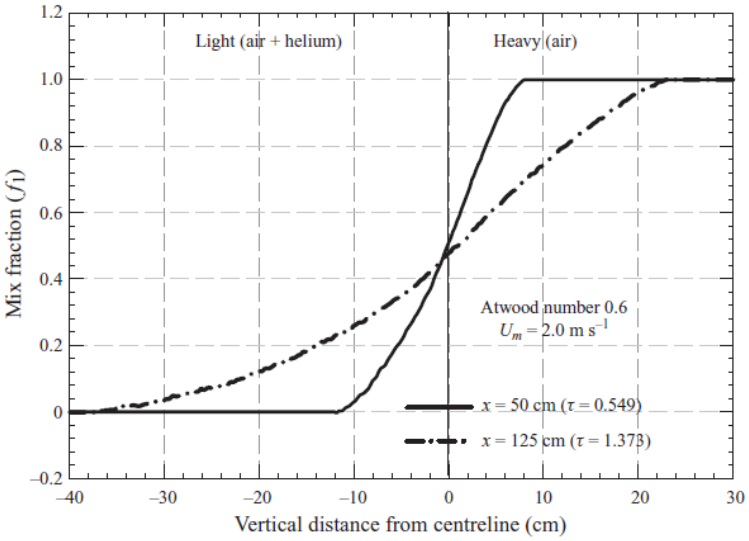

Figure 2.8. Plot of mixing width fraction versus distance from centerline for two axial locations.

Since the channel is convective in nature, the flow is steady in time but not in space as the instability continues to develop as the fluid moves downstream. This statistically steady hydrodynamic instability allows for large data collection times to be studied. Fog is added to the bottom stream for visualization and for aid in determining the volume fractions. Using a wedge calibration system, with the bottom stream having the least intensity and the top stream the most, the mixture fraction and growth rates throughout the flow field can be determined using ensemble averaging of captured images. Velocity and density information at certain points throughout the flow field can be obtained from hot wire anemometry data, and temperature information can be obtained from thermocouples.

2.5.2 Description of problem setup

To model this experiment, a computational box with dimensions 0.3 m x 0.3 m x 1.2 m was created with grid spacing of 128 x 64 x 512 to provide a resolution of 2.344 mm x 4.688 mm x 2.344 mm in the x, y, and z dimensions, respectively. The top fluid was set to have a density of 1.14 kg/m^3 and a velocity of 2 m/s while the bottom fluid was given a density of 0.285 kg/m^3 and velocity of 2 m/s. The program was set to run for a physical time of 1 s with 55000 time steps, which took 2.5 hours to complete, and was given the same perturbation as in the White *et al.* case since the gas channel does not have well defined initial conditions. The x and y planar boundaries were set to be cyclic as the physical dimensions would require too much computational power to model exactly.

2.5.3 Results from computational code

The bubble and spike heights based on 5% and 95% volume fractions are shown versus the distance from the splitter plate in Figure 2.9. Comparing this image with Figure 2.8, at 50 cm the mixing width is nearly the same, with a value of approximately 16 cm for the experiment and 13 cm for the model. Further down the channel, however, the computation seems to saturate while the experiment continues to grow exponentially, leading to a height of 50 cm for the experiment versus 33cm for the computation at a distance of 125 cm. Looking at an image developing throughout the run, the mushroom structures are much more developed than in the 0.46 Atwood number case (see Figure 2.10). Comparing to Figure 2.7, the mixing width in both instances is larger on the left side of the image, showing that the Rayleigh-Taylor instability is causing the fluids to mix as they move downstream.

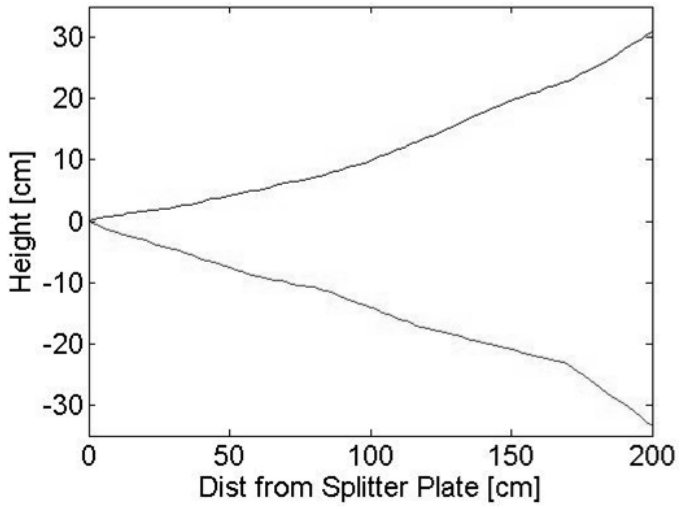

Figure 2.9. Mixing width based on 5% and 95% volume fractions for Atwood number 0.6 case.

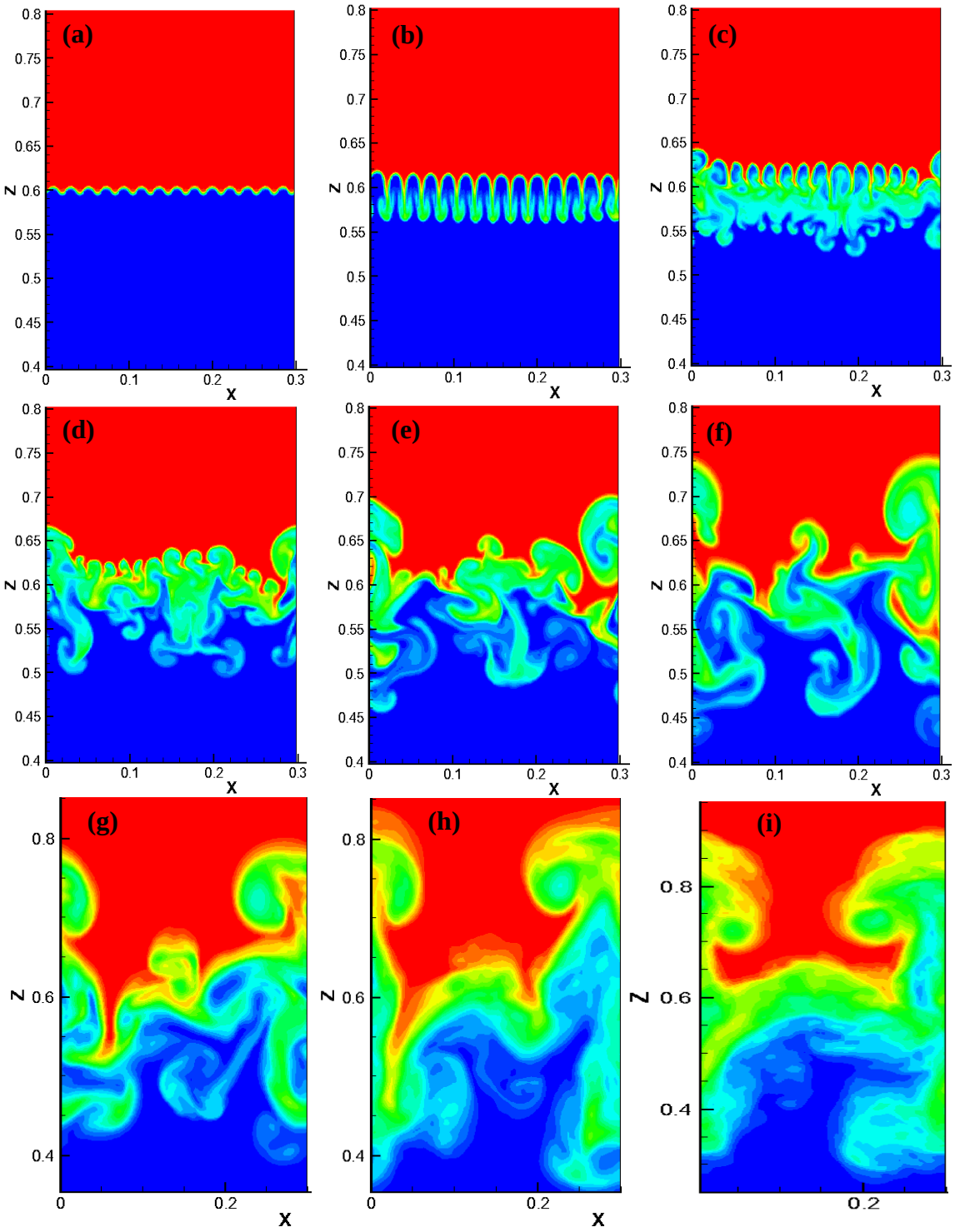

Figure 2.10. Image taken equivalent to a distance of (a) 2 cm, (b) 26 cm, (c) 52 cm, (d) 76 cm, (e) 102 cm, (f) 126 cm, (g) 152 cm, (h) 176 cm, (i) 200 cm from the splitter plate for Atwood number 0.6 case.

2.6 Comparison to Texas A&M University Experiment, Atwood Number 0.032

The final goal of this segment was to model a low Atwood number case since the accuracy of the medium and high numbers has been validated. For this reason, a pure Rayleigh-Taylor case with Atwood number of 0.032, based on Akula *et al.*'s paper with an Atwood number of 0.035 also dealing with the gas channel, was selected (Akula *et al.* 2012).

2.6.1 Description of physical experiment

The experimental facility utilized in this work is the same as was operated in Banerjee *et al.*'s paper. The top fluid is still pure air with density of 1.14 kg/m^3 but is now moving with a velocity of 0.63 m/s. The bottom fluid only needs enough helium to create a density of 1.063 kg/m^3 and is also moving with a velocity of 0.63 m/s. A picture of the run can be seen in Figure 2.11 while an image of the mixing width throughout the channel is shown in Figure 2.12.

Figure 2.11. Image of test section from gas channel with Atwood number 0.035.

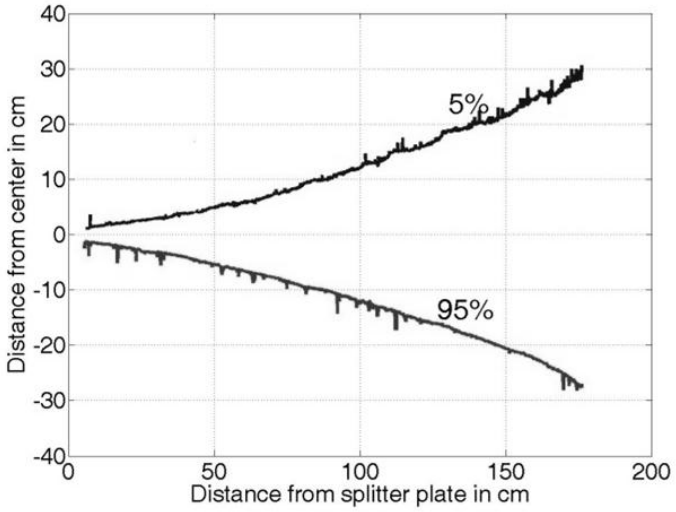

Figure 2.12. Mixing width based on 5% and 95% volume fractions for Atwood number 0.035.

2.6.2 Description of problem setup

To model this experiment computationally, a box with dimensions 0.3 m x 0.3 m x 1.2 m was created with grid spacing of 128 x 64 x 512 to provide a resolution of 2.344 mm x 4.688 mm x 2.344 mm in the x, y, and z dimensions, respectively. The top fluid was set to have a density of 1.14 kg/m^3 and a velocity of 1 m/s while the bottom fluid was given a density of 1.07 kg/m^3 and velocity of 1 m/s. This provided the system with an Atwood number of 0.032 and no shear in the system. The program was set to run for a physical time of 3 s with 85000 time steps, which took 3.5 hours to complete, and was given the same perturbation as in the White *et al.* case since the gas channel does not have well defined initial conditions. The x and y planar boundaries were set to be cyclic as the physical dimensions would require too much computational power to model exactly.

2.6.3 Results from computational code

Comparing the mixing width of the computational run (Figure 2.13) to that from the experiment (Figure 2.12), the former is shown to be much smaller than the latter at nearly a third of the value. This information suggests that the initial interface perturbations are not adequate for recreating the experimental data. Comparing the flow development throughout the test section (Figure 2.14) to the previous images of the computational run, the mushrooms in the Atwood number 0.032 case are much less developed than the two higher Atwood number cases.

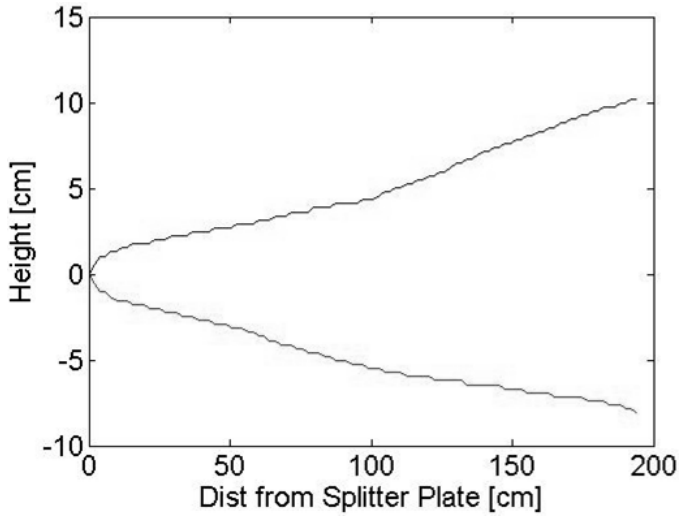

Figure 2.13. Mixing width based on 5% and 95% volume fractions for Atwood number 0.032 case.

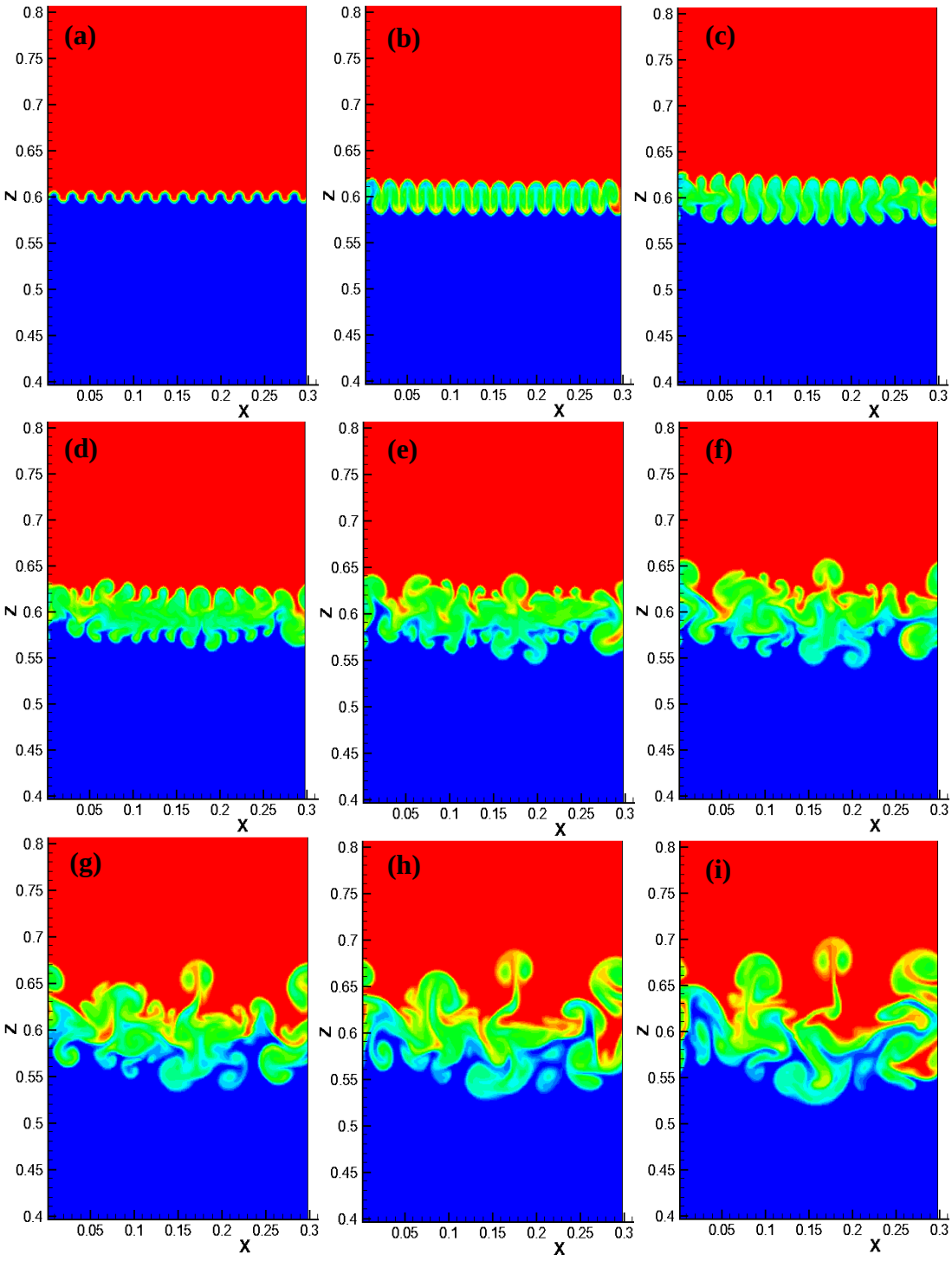

Figure 2.14. Image taken equivalent to a distance of (a) 1.94 cm, (b) 25.22 cm, (c) 50.44 cm, (d) 73.72 cm, (e) 98.94 cm, (f) 122.22 cm, (g) 147.44 cm, (h) 170.72 cm, (i) 194 cm from the splitter plate for Atwood number 0.032 case.

2.7 Comparison of Atwood Number 0.6 to Atwood Number 0.032

Since the works of Banerjee *et al.* and Akula *et al.* utilize the same experimental facility, it is easy and beneficial to compare the two cases in order to analyze the effect of Atwood number on fluid mixing. Figure 2.15 illustrates the total mixing width versus distance from splitter plate for both Atwood numbers. As can be seen, the amount of mixing greatly increasing when the density difference between the two fluids is larger.

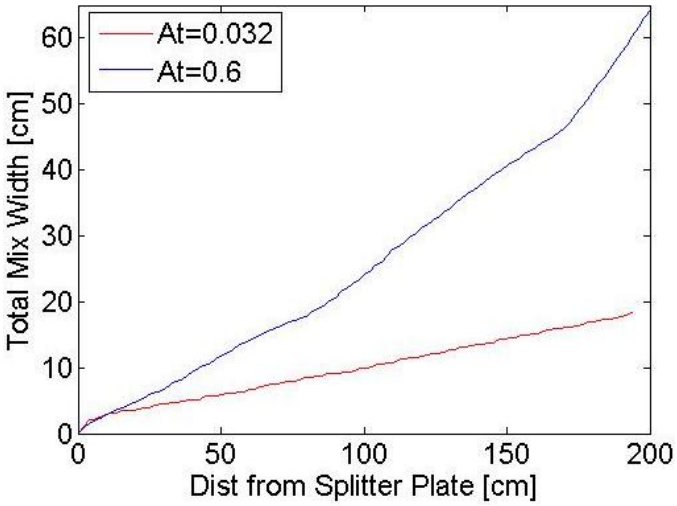

Figure 2.15. Total mixing width comparison of Atwood numbers 0.6 and 0.032.

An alternative way to inspect the fluid amalgamation is to look at the molecular mixing parameter θ. In order to better compare the two Atwood numbers, the time from the start of mixing is nondimensionalized as

$$\tau = t\sqrt{\frac{A_t * g}{H}} \tag{2.24}$$

where t is the time after the start of the run and H is the total height of the channel. The plot of this value measured at the centerline can be seen in Figure 2.16 and depicts the lower Atwood number case as having a higher value. This circumstance illustrates that while the Atwood number 0.6 case has a higher mixing width, there is more molecular mixing occurring in the Atwood number 0.032 case. Thus, the degree of mixing in each fluid is different for each case depending on whether molecular or macroscopic amalgamation is the parameter of interest.

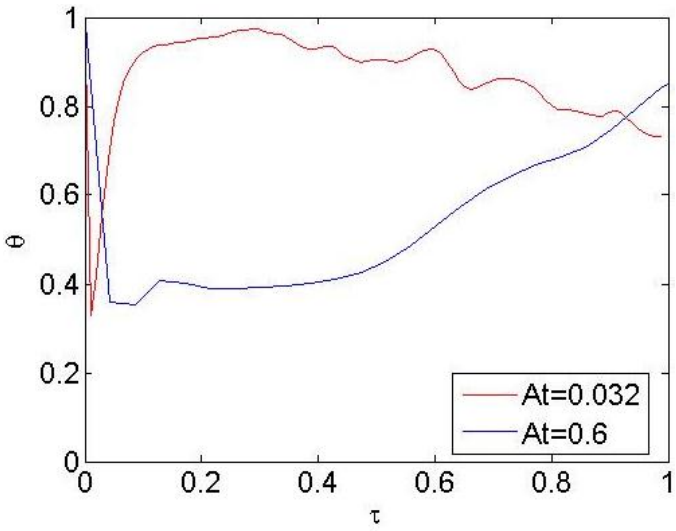

Figure 2.16. Comparison of molecular mixing at the centerline versus nondimensionalized time for Atwood numbers 0.6 and 0.032.

3. ALTERNATIVE INITIAL INTERFACE CONDITIONS AND THE EFFECT OF SHEAR ON THE SYSTEM

3.1 Overview of Goals and Methodology

With the code validated and pure Rayleigh-Taylor instabilities investigated, the next step was to modify the boundary perturbation to better represent the physical experiments whose fluid interfaces were not clearly defined. In order to accomplish this task, hot wire anemometry was used on the gas channel to collect velocity and density data, which were then transformed into a power spectrum to provide insight into the energy delivered to the interface. The two methods of modeling the interface were then compared for the parameters of mixing width, and θ.

Next, the power spectrum was further investigated by looking at initial velocity fluctuations that do not appear in the spectrum data. Different fractions of fluctuations obtained from hot wire anemometry were compared in order to determine which provided the most realistic representation of the results. Experimental data was compared against the different fluctuations for mixing width and mixing width gradient. The latter is utilized to determine the magnitude of Rayleigh-Taylor, which grows exponentially, and Kelvin-Helmholtz, which grows linearly, effects on the flow.

Finally, the level of shear in the system was increased in order to determine the effect of this condition on fluid mixing. Seven cases were investigated, one with no velocity (Atwood number 0.032), one with no density difference (shear of 0.8 m/s) and five cases with intermediate levels of shear (0.2 m/s, 0.35 m/s, 0.5 m/s, 0.65 m/s and 0.8 m/s) and Atwood number 0.032. The growth parameter, mixing width, molecular

mixing, Richardson number, and Reynolds number were compared, as well as how the mixing width gradient changes with regard to the Richardson number. The growth parameter α can be found by solving for the value directly from equation 1.1 and gives

$$\alpha_{b,s} = \frac{h_{b,s}}{A_t g t^2} \tag{3.1}$$

while the Richardson number is the ratio of potential to kinetic energy, equivalent to the ratio of Rayleigh-Taylor to Kelvin-Helmholtz effects, and can be described by

$$Ri = \frac{-g\left(\frac{\partial \rho}{\partial z}\right)}{\rho\left(\frac{\partial u}{\partial z}\right)^2} = \frac{-2*h*g*\Delta\rho}{\bar{\rho}*\Delta U^2} \tag{3.2}$$

where the negative sign used for the definition of unstably stratified flows.

3.2 Single versus Multimode Interface Perturbation

The first step taken to ensure a realistic interface perturbation was to obtain hot wire data from the physical gas channel experiment. From this information, the computational code was modified and ran with various cases of shear to compare the differences between the two methods.

3.2.1 Obtaining the power spectrum and subsequent code modification

Hot wire anemometry can be broken into two categories: constant current or constant temperature. For constant current, the change in voltage is due to a change in resistance, which is indirectly related to a change in temperature. For constant temperature, a specific resistance for the system is set, and the resulting voltage change through the wire is measured. For both systems, calibration curves must be created in order to determine the relationship between the measured voltage and system's density or

velocity, respectively, for each specific experimental variation. These variations include overheat ratio, fraction of different gasses, etc.

For a constant temperature system, a calibration scheme must be used to obtain the parameters in King's Law ($E^2=bU^{0.5}$) where U is the known input velocity, E is the resulting voltage values from the hot wire probe, and b is the calibration constant. It is also highly critical to ensure the hot wire is lined up with the flow field so that the proper calibration relationship is obtained. Once the square root of the known calibration mean velocity data is plotted versus the resulting squared voltage values, a line of best fit can be used to obtain the parameter b. Again, these values are only for the specific variations in which they are measured, and multiple calibration curves for all combinations of variations must be obtained. This requirement results in different values of parameter b depending on the percentage of helium in the system (and thus the Atwood number). Proceeding in this manner, all appropriate calibration curves were acquired for the various Atwood numbers, and the gas channel experiment was conducted with a three wire constant temperature hot wire to find the velocity from King's Law as now the voltage and b are known.

With the velocities U_1, U_2, and U_3 at each of the three probes now obtained, the x, y, and z components of the flow velocity at the measured location can be found. The equalities for these values for gold plated hot wire sensors can be seen in equations (3.3) to (3.5), respectively.

$$U = U_1 * \cos(54.74) + U_2 * \cos(54.74) + U_3 * \cos(54.74) \quad (3.3)$$

$$V = -U_1 * \cos(45) - U_2 * \cos(135) + U_3 * \cos(90) \quad (3.4)$$

$$W = -U_1 * \cos(114.09) - U_2 * \cos(114.09) - U_3 * \cos(35.26) \quad (3.5)$$

A single wire constant current hot wire was utilized to obtain the temperature at the same point as the three probe constant temperature hot wire, which was then related to the density from the calibration data. Both anemometry measurements were taken half an inch from the splitter plate in order to best determine the initial conditions of the fluids upon their first interaction (see Figure 3.1).

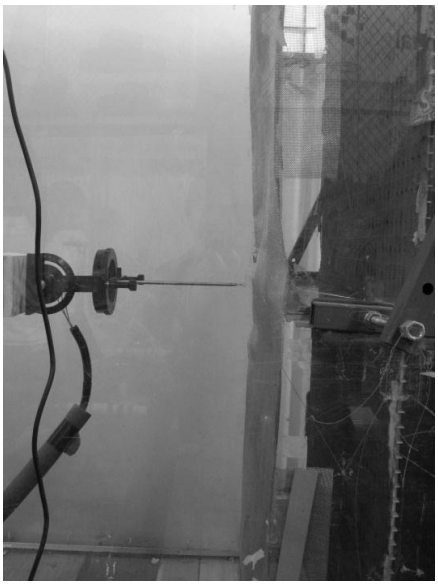

Figure 3.1. Image of hot wire anemometer collecting data half an inch from the splitter plate in the gas channel.

Using the density information gained from the hot wire anemometry, a fast Fourier transform of the density fluctuations was obtained for half of the measured values due to the limitations of the Nyquist frequency. This method produced a plot of the density power spectrum versus wavenumber that was then used to create the

multimode perturbation (Figure 3.2). Of the power spectrum data collected, wavelengths up to 4Δx (9.376 mm) can be used, after which point the viscosity damps out the eddies. This value is equivalent to a wavenumber of $\pi/2\Delta x$ or 0.67 mm^{-1}. The equation for the velocity perturbation then becomes:

$$M_k = \sqrt{a * k^b} * \text{sgn} * \sin(k * x) * e^{-k*|z|}/k \tag{3.6}$$

where k is the current wavenumber, M_k is the mode at that wavenumber, b is the slope at that wavenumber, and a is the value when k = 1.

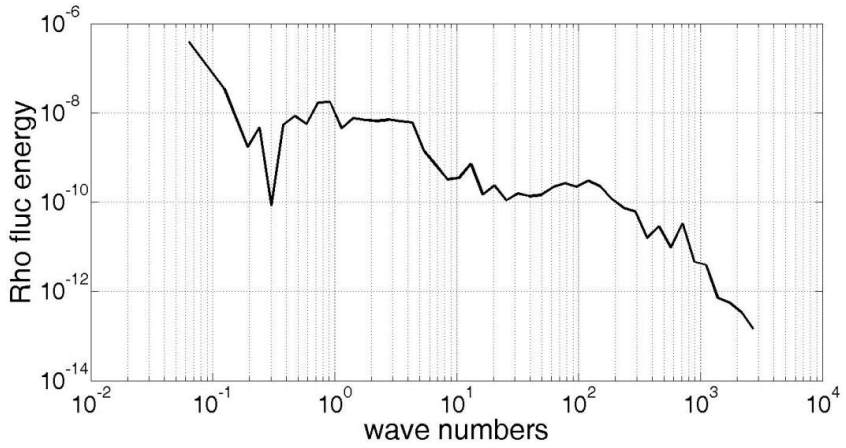

Figure 3.2. Density power spectrum obtained half an inch from the splitter plate in the Texas A&M University gas channel.

From the physical data collected, a number of changes were implemented into the computational code besides those listed above for the interface perturbation. As with the previous Atwood number 0.032 case, a box with dimensions 0.3 m x 0.3 m x 1.2 m was created with grid spacing of 128 x 64 x 512 to provide a resolution of 2.344 mm x 4.688 mm x 2.344 mm in the x, y, and z dimensions, respectively. The top fluid was set

to have a density of 1.14 kg/m^3 and a velocity of 1 m/s while the bottom fluid was given a density of 1.07 kg/m^3 and velocity 1 m/s. This assignment provided the system with an Atwood number of 0.032 and no shear, in other words a pure Rayleigh-Taylor arrangement. The program was set to run for a physical time of 3 s with 85000 time steps and took 5.5 hours to complete. The x and y planar boundaries were set to be cyclic as the physical dimensions would require too much computational power to model exactly.

3.2.2 Results from computational code

The total computational mixing width can be seen in Figure 3.3 and is about half of that in the physical experiment shown in Figure 2.12. Images throughout the gas channel are shown in Figure 3.4. As can be seen, a few of modes dominate while smaller modes continue to develop in their midst. These dominant modes will continue to grow and will soon take over the smaller structures.

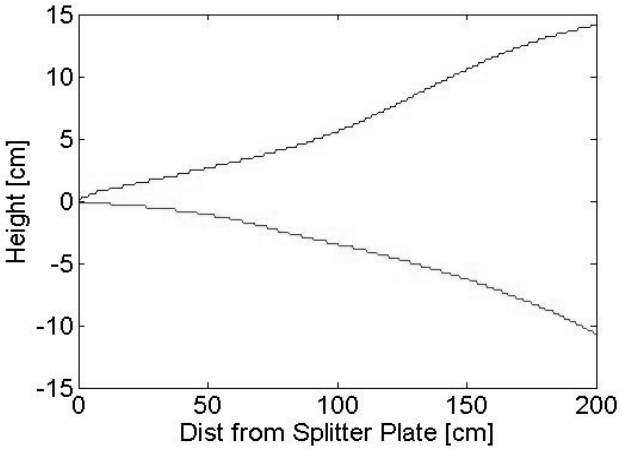

Figure 3.3. Mixing width based on 5% and 95% volume fractions for no shear Atwood number 0.032 case with power spectrum interface perturbation.

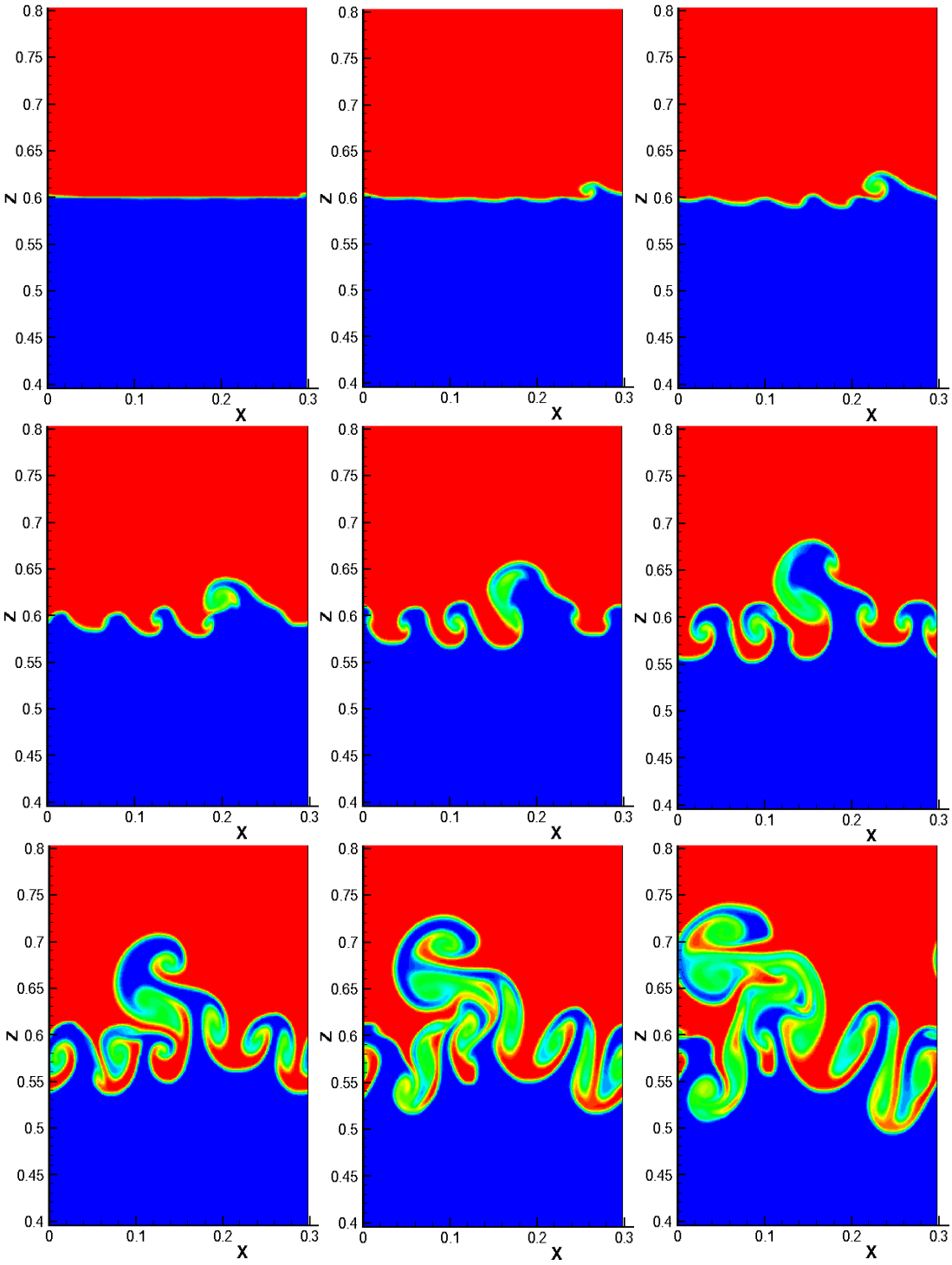

Figure 3.4. Image taken an equivalent distance of (a) 3.6 cm, (b) 28.2 cm, (c) 53.4 cm, (d) 78 cm, (e) 103.2 cm, (f) 127.8 cm, (g) 153 cm, (h) 177.6 cm, (i) 199.8 cm from splitter plate for the Atwood number 0.032 power spectrum case.

In spite of this fact, however, the gradient of the mixing width (Figure 3.5) grows linearly, indicating parabolic growth of the mixing width which is typical of Rayleigh-Taylor instabilities. The linear growth stops around 140 cm past the splitter plate and transitions to a constant value. This growth in the height gradient is indicative of a linear evolution of the mixing width, characteristic of Kelvin-Helmholtz instability, and illustrates a saturation of the Rayleigh-Taylor bubble growth. Because of this saturation, code involving density instabilities is only valid up to 140 cm from the splitter plate. The height gradient from the physical experiment in Section 2.5 can be seen in Figure 3.6 and shows the same linear growth as the computational run.

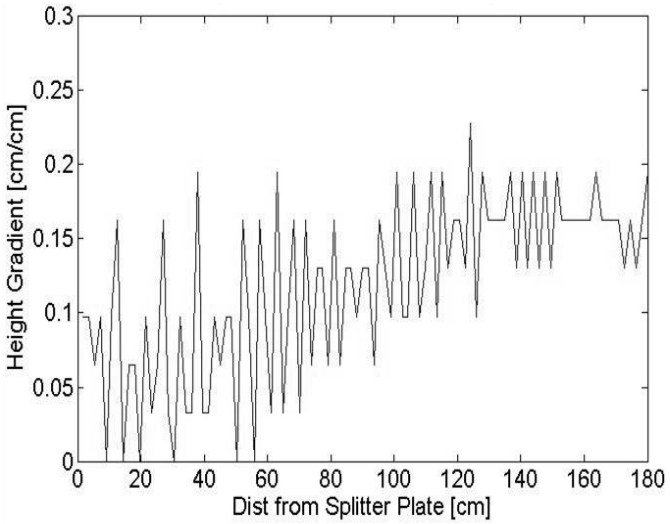

Figure 3.5. Mixing width height gradient for no shear Atwood number 0.032 case with power spectrum interface perturbation.

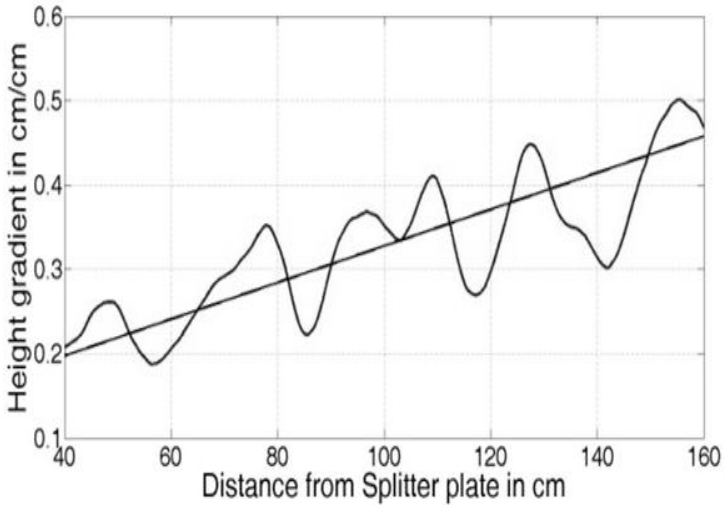

Figure 3.6. Mixing width height gradient for no shear Atwood number 0.035 experimental data.

3.2.3 Comparison of single and multimode perturbation

Comparing the mixing widths of the single and multiple sine wave interface perturbation results in the image shown in Figure 3.7. At first the single mode has a greater mixing width, but around 120 cm past the splitter plate the multimode case overtakes. This switch can be attributed to the parabolic growth seen in the power spectrum scenario, which matches better with theory and experiments for pure Rayleigh-Taylor data. Further, because of this greater rate of growth, the total mixing width of the density spectrum matches closer to physical experiments.

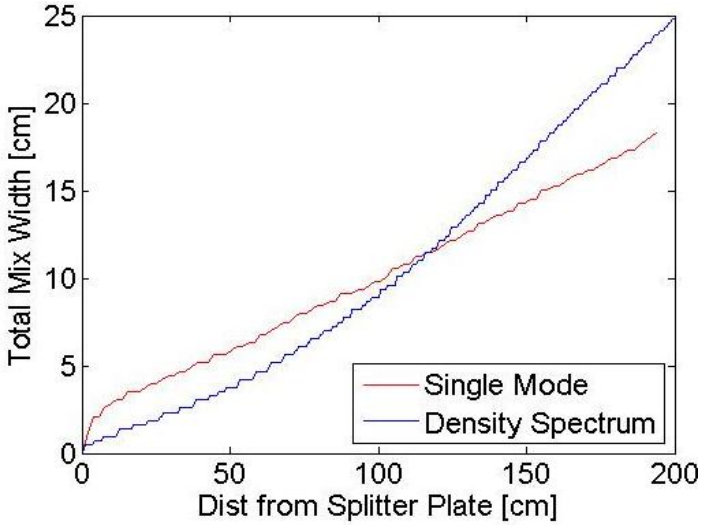

Figure 3.7. Comparison of mixing width with a single and multimode interface perturbation with no shear and Atwood number 0.032.

An alternative manner in which to compare the two cases is to investigate the level of molecular mixing at the centerline (Figure 3.8). As with before, one scenario has a smaller mixing width but larger molecular mixing and the other the opposite. Due to the accuracy of the power spectrum height gradient compared to physical data and theory, this case provides a better computational representation of the physical happenings and will be used from here on out.

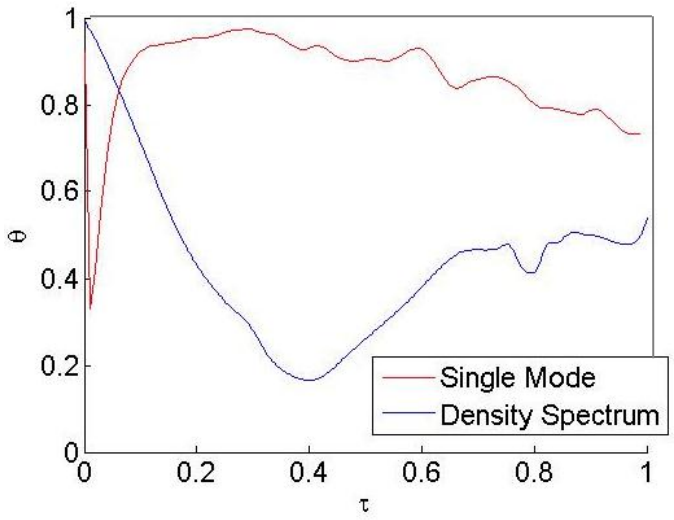

Figure 3.8. Comparison of molecular mixing at the centerline versus nondimensionalized time for single and density spectrum fluid interface perturbation for no shear Atwood number 0.032.

3.3 Vertical Velocity Fluctuations in Power Spectrum Perturbation

With pure Rayleigh-Taylor instabilities fully investigated, a pure Kelvin-Helmholtz case was explored. However, when the code was computed using the aforementioned techniques, the bubble and spike growth stagnated prior than it theoretically should have. Investigation into the code suggested an insufficiency in the input vertical energy which drives the Kelvin-Helmholtz instability. Thus, a parametric study with four levels of vertical velocity fluctuation was conducted in order to determine which method provided the most realistic results.

3.3.1 Obtaining velocity fluctuations and subsequent code modification

The data used to determine the best velocity fluctuation in the computational code was the hot wire anemometry data obtained in Section 3.2. From measurements taken at 0.5

and 1.5 inches from the splitter plate, linear interpolation was used to find the velocity fluctuation at the splitter plate. This value was found to be (0.0856, 0.05665, 0.06240) m/s in the x, y, and z directions, respectively. To implement this into the code, the numbers were simply added onto the original velocity components for the top and bottom fluids. As the vertical component is the most important, variations of a half, fourth, and eighth of this component were also modeled with the other two components held constant.

Similar to the previous cases, to model this shear instability a computational box with dimensions 0.3 m x 0.3 m x 1.2 m was created with grid spacing of 128 x 64 x 512 to provide a resolution of 2.344 mm x 4.688 mm x 2.344 mm in the x, y, and z dimensions, respectively. The top fluid was set to have a density of 1.14 kg/m^3 and a velocity of 1 m/s while the bottom fluid was given a density of 1.14 kg/m^3 and velocity of 0.2 m/s. The program was set to run for a physical time of 3 s with 55000 time steps, and the completion time ranged from 5.25 to 7 hours for the four different fluctuations. The x and y planar boundaries were set to be cyclic as the physical dimensions would require too much computational power to model exactly.

3.3.2 Results from computational code

The mixing width from the Texas A&M University gas channel experiment with shear of 0.65 m/s is shown in Figure 3.9 (Akula *et al.* 2012). The initial mixing width prior to the addition of velocity fluctuations can be seen in Figure 3.10; the mixing widths for the four velocity fluctuations can be seen in Figure 3.11. While the initial run stops its linear growth around 60cm, the updated code has a near-constant linear growth.

However, the mixing width is about twice as large in the presence of velocity fluctuations, regardless of the magnitude of the vertical value, than in the previous case with no fluctuation. Comparing to the experimental data, the mixing width matches best with the case without velocity fluctuations, but the linear growth matches best with the velocity fluctuation methods.

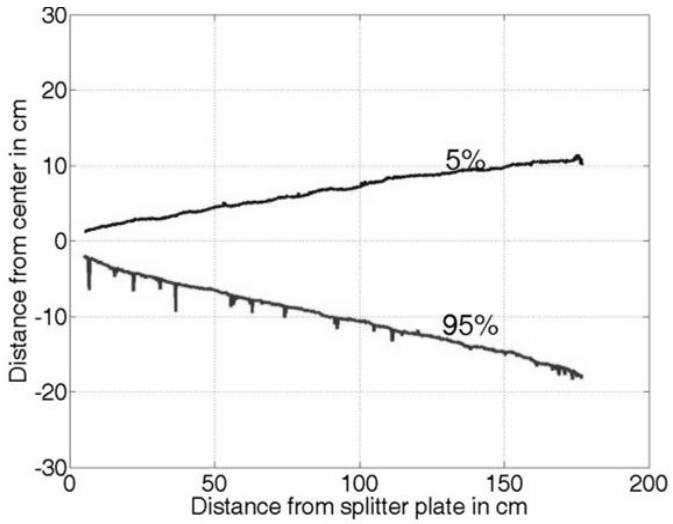

Figure 3.9. Mixing width from Kelvin-Helmholtz experimental data with shear of 0.65 m/s.

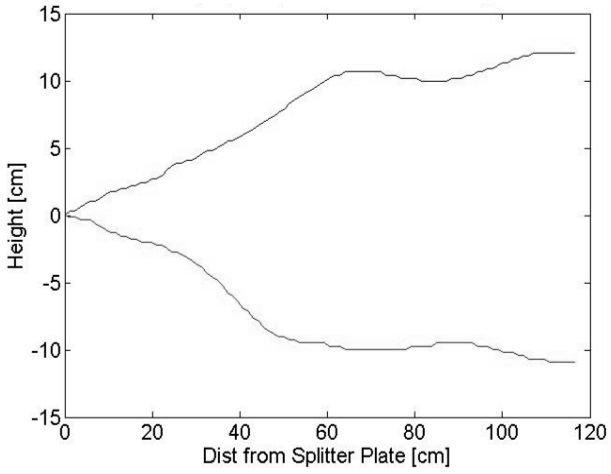

Figure 3.10. Mixing width of Kelvin-Helmholtz instability with no velocity fluctuations.

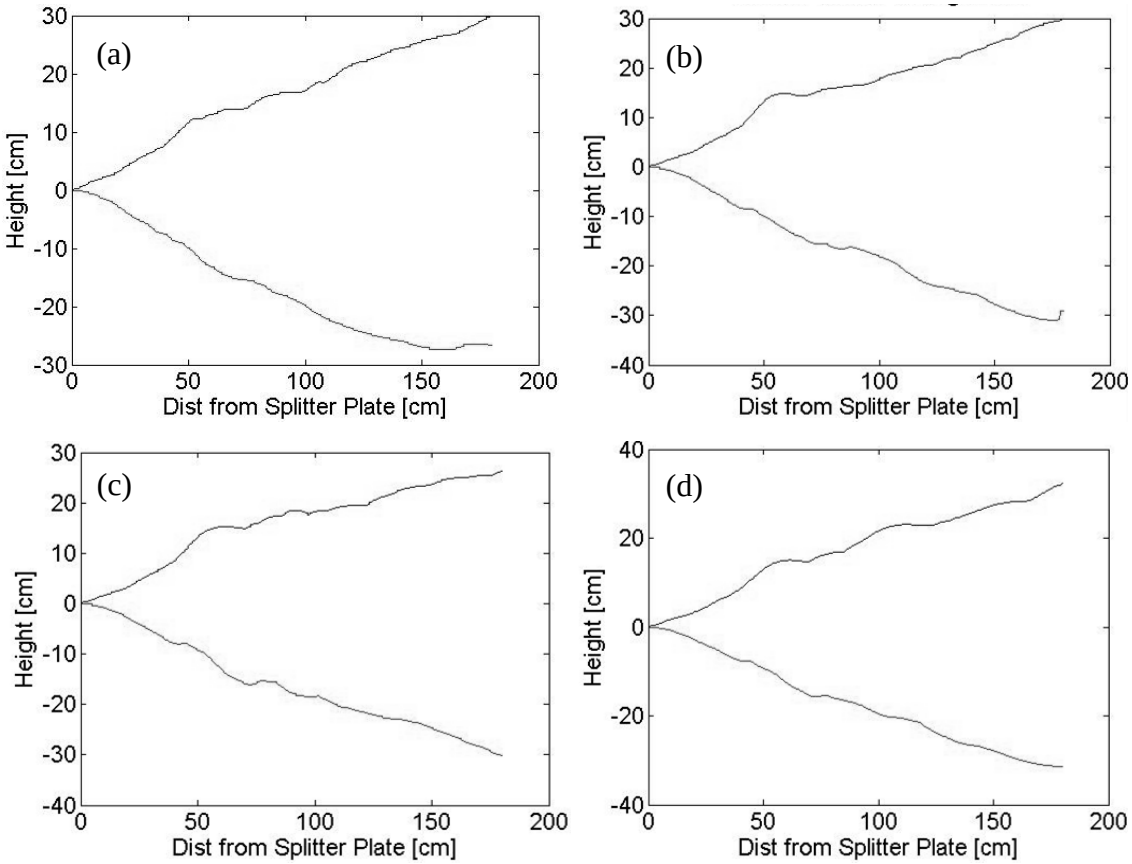

Figure 3.11. Mixing width of Kelvin-Helmholtz instability with vertical velocity fluctuation of (a) full, (b) half, (c) quarter, and (d) eighth value.

A better way to visualize the linear growth characteristic of Kelvin-Helmholtz instability is by comparing the height gradients of the mixing widths to each other and to the physical experiment. The former can be seen in Figure 3.12 and the latter in Figure 3.13. While the experimental height gradient has a value around 0.15 cm/cm, the computational data ranges near 0.25 cm/cm and decreases slightly as the vertical velocity is decreased. Regardless, all fluctuation cases possess the near-constant growth of the height gradient, corresponding to a linear growth of the mixing width, which is characteristic of the Kelvin-Helmholtz instability. For this reason, the velocity fluctuation method is best for modeling shear instabilities.

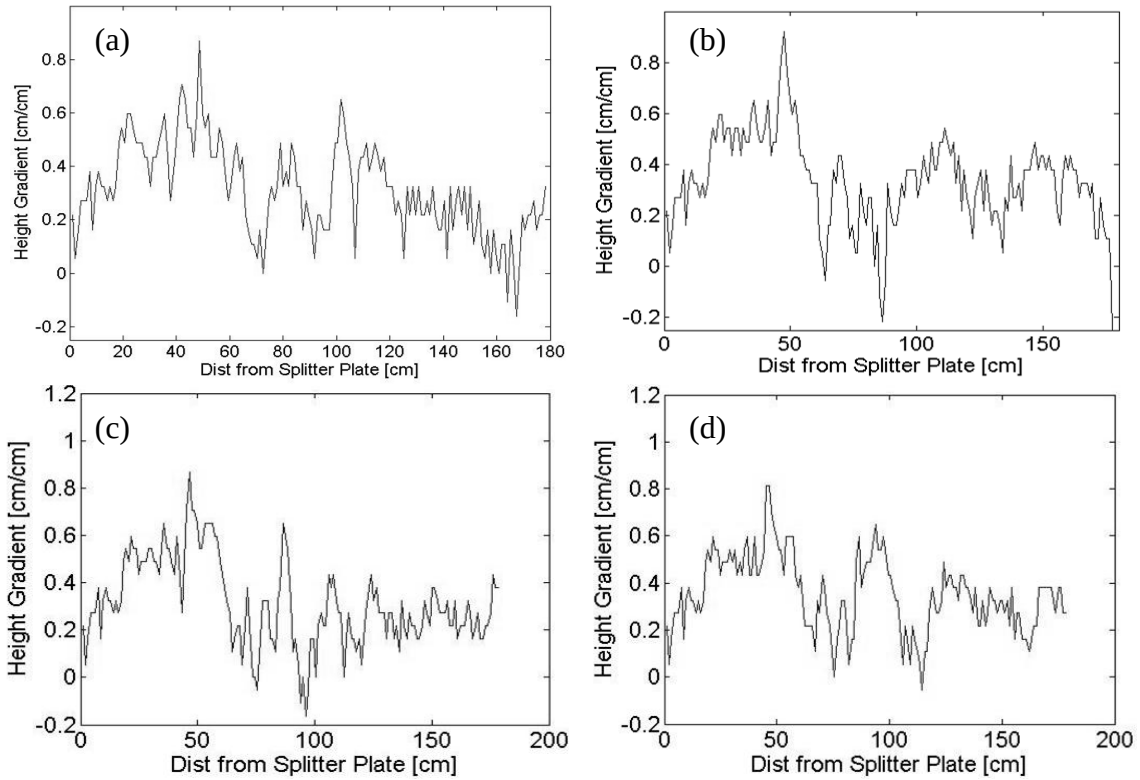

Figure 3.12. Mixing width height gradient of Kelvin-Helmholtz instability with vertical velocity fluctuation of (a) full, (b) half, (c) quarter, and (d) eighth value.

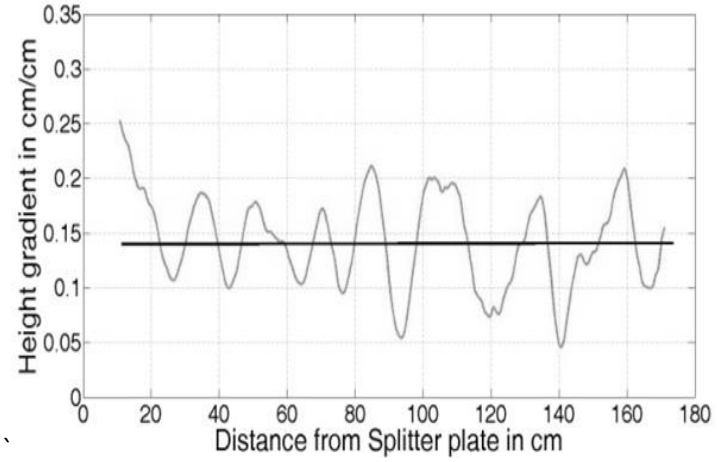

Figure 3.13. Height gradient of experimental shear instability with shear of 0.65 m/s.

Finally, the total mixing widths of the four velocity fluctuation cases were compared on one plot (Figure 3.14). The methods are near identical up to 50cm from the splitter plate, but then begin to spread out. The fractions of the linear interpolation case present on either side of the whole value of the mixing width. In order to determine which method provides the most accurate results, experiment and theory can be recalled. Comparing the mixing widths to the former, a smaller mixing width is ideal. Comparing the height gradient to the latter, a constant value matches best with Kelvin-Helmholtz instability. The method which provides the best fit for these criteria is the full valued vertical velocity fluctuation.

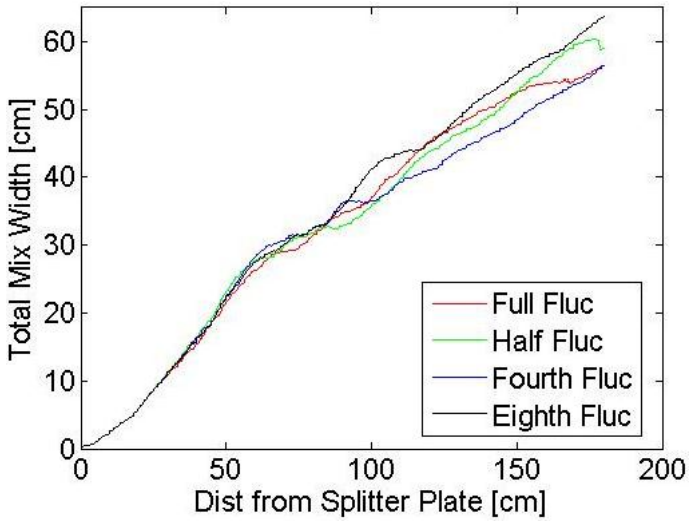

Figure 3.14. Total mixing widths for four vertical velocity fluctuations in shear instability.

3.4 Effect of Increased Shear on Rayleigh-Taylor Kelvin-Helmholtz Instability

With both Rayleigh-Taylor and Kelvin-Helmholtz cases now fully explored, intermediate cases with both instabilities were investigated. The two extremes of no shear with density difference (Section 3.2) and shear with no density difference (Section 3.3) were used with five intermediate cases where the shear was increased from 0 m/s to 0.8 m/s.

3.4.1 Code modification

For all five intermediate cases, a box with dimensions 0.3 m x 0.3 m x 1.2 m was created with grid spacing of 128 x 64 x 512 to provide a resolution of 2.344 mm x 4.688 mm x 2.344 mm in the x, y, and z dimensions, respectively. The top fluid was set to have a density of 1.14 kg/m^3 and a velocity of 1 m/s while the bottom fluid was given a density of 1.07 kg/m^3 and velocity ranging from 0.8 m/s to 0.2 m/s in five decrements. This

provided the system with an Atwood number of 0.032 and a shear in the system 0.2 m/s, 0.35 m/s, 0.5 m/s, 0.65 m/s, and 0.8 m/s. The program was set to run for a physical time of 3 s with 85000 time steps, and completion time ranged from to 5.25 to 6.25 hours for the five cases. The x and y planar boundaries were set to be cyclic as the physical dimensions would require too much computational power to model exactly.

3.4.2 Results from computational code

Images from the computational run taken an equivalent distance of 2 cm (Figure 3.15), 60 cm (Figure 3.16), and 200 cm (Figure 3.17) from the splitter plate can be seen for the increasing levels of shear along with the pure Kelvin-Helmholtz case with the full velocity fluctuation. As the shear in the system increases, the rollup structures become more and more dominant, illustrating the greater influence of Kelvin-Helmholz effects in the flow. The increase in shear effects can further be seen by comparing how the Richardson number changes with distance from the splitter plate (Figure 3.18). As the shear increases in the system, the Richardson number decreases. Since this value is the ratio of Rayleigh-Taylor to Kelvin-Helmholtz effects, this trend indicates that the Kelvin-Helmholtz impact is increasing. Note that the pure Rayleigh-Taylor and pure Kelvin-Helmholtz case is not present Figure 3.16 as the value of the former is undefined and the latter is zero.

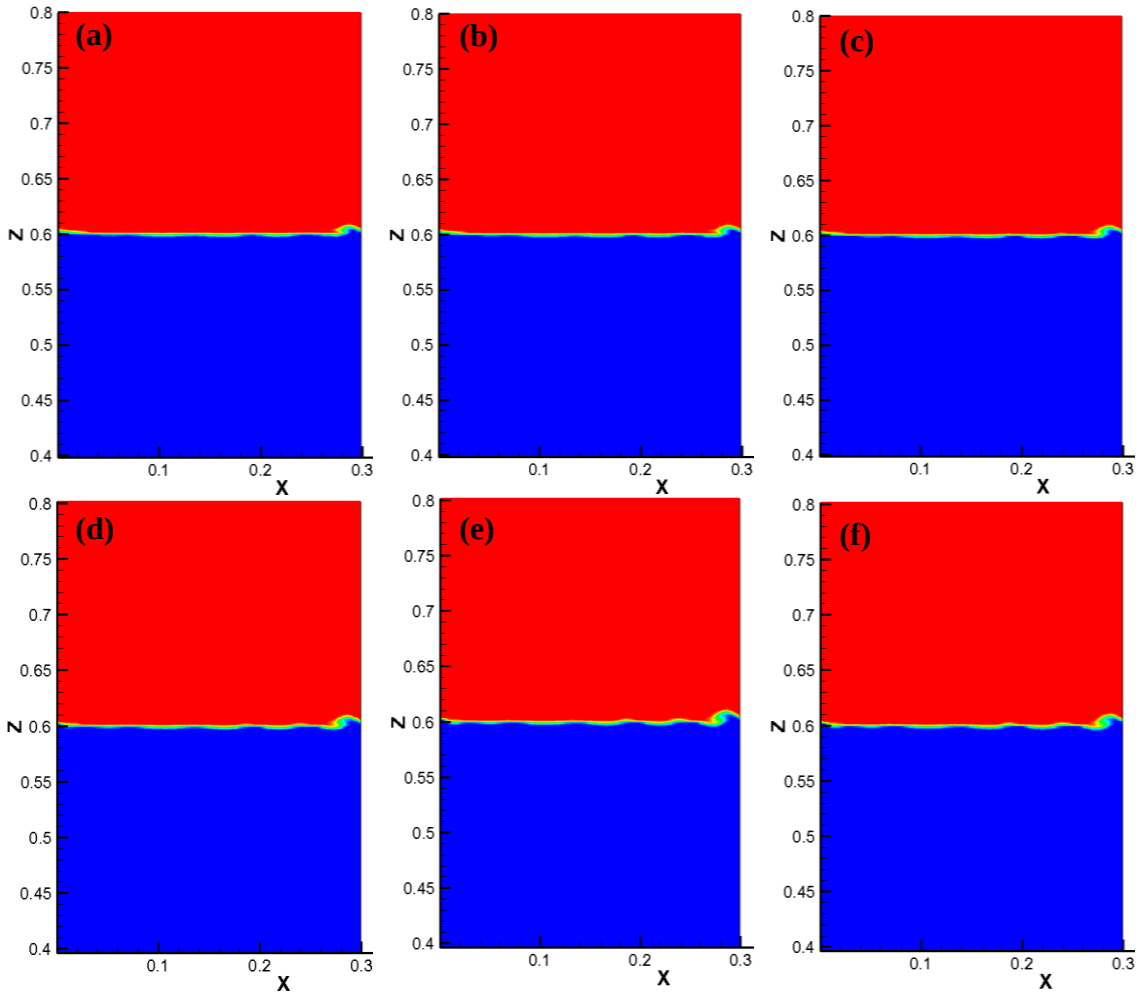

Figure 3.15. Image of computational run equivalent to 10 cm from the splitter plate for Atwood number 0.032 and shear of (a) 0.2 m/s, (b) 0.35 m/s, (c) 0.5 m/s, (d) 0.65 m/s, (e) 0.8 m/s, and (f) Kelvin-Helmholtz shear of 0.8 m/s.

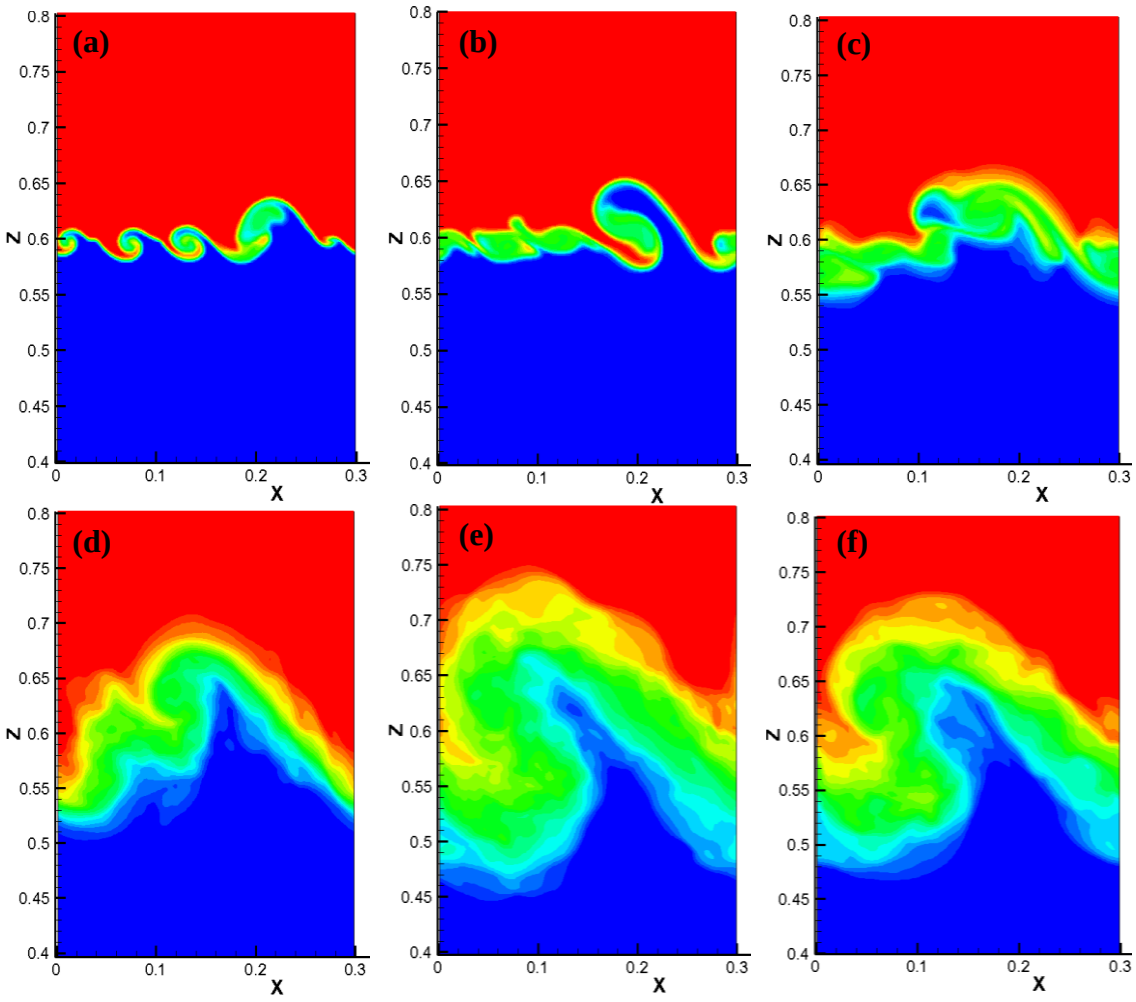

Figure 3.16. Image of computational run equivalent to 60 cm from the splitter plate for Atwood number 0.032 and shear of (a) 0.2 m/s, (b) 0.35 m/s, (c) 0.5 m/s, (d) 0.65 m/s, (e) 0.8 m/s, and (f) Kelvin-Helmholtz shear of 0.8 m/s.

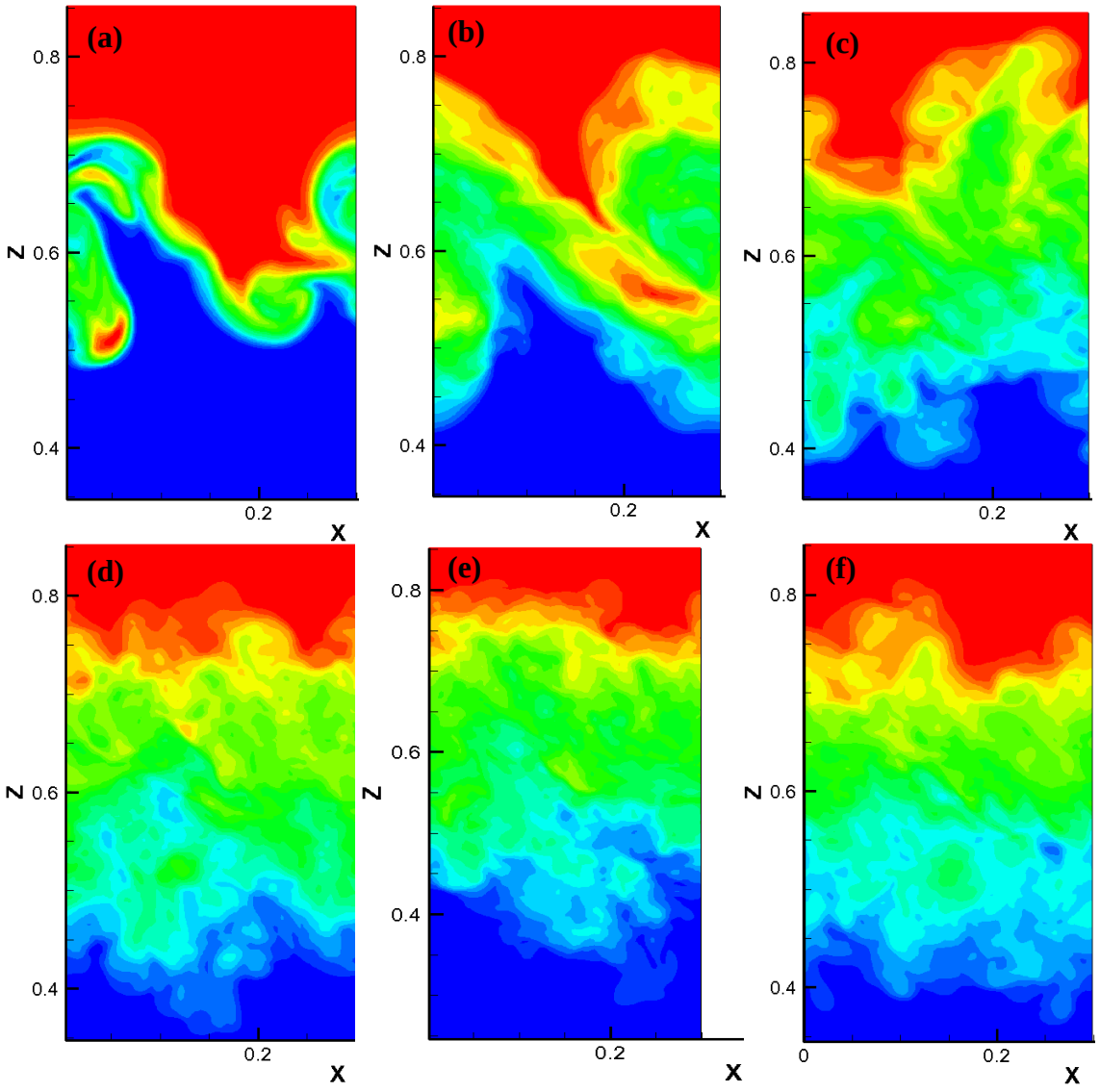

Figure 3.17. Image of computational run equivalent to 200 cm from the splitter plate for Atwood number 0.032 and shear of (a) 0.2 m/s, (b) 0.35 m/s, (c) 0.5 m/s, (d) 0.65 m/s, (e) 0.8 m/s, and (f) Kelvin-Helmholtz shear of 0.8 m/s.

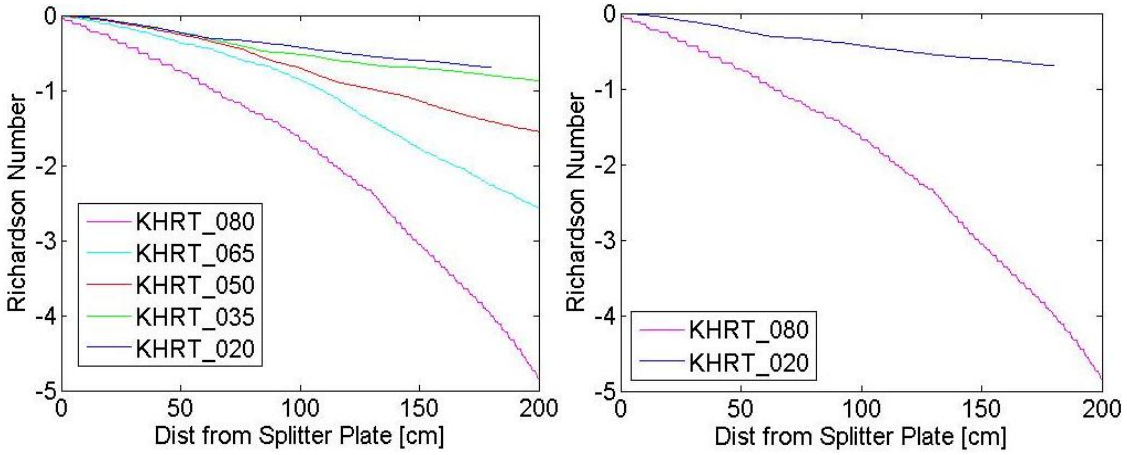

Figure 3.18. Plot of Richardson number as it changes from the splitter plate, where KHRT_0## corresponds to the Rayleigh-Taylor Kelvin-Helmholtz combined instability with bottom velocity 0.## (ex: KHRT_080, bottom velocity 0.8 m/s).

The mixing in the various levels of shear can be seen in the mixing widths and level of molecular mixing for the seven cases (Figure 3.19 and 3.20, respectively). As the shear in the system increases, the mixing width subsequently increases. This element is because the time required for the parabolic growth of the Rayleigh-Taylor instability to take over the linear growth of the Kelvin-Helmholtz instability has not yet been reached. When the density difference between the two fluids is removed, the mixing width decreases versus the same shear with a density gradient. This detail can be explained by the energy put into the amalgamation due to the instability. The Kelvin-Helmholtz Rayleigh-Taylor instability has two instabilities, causing it to mix more than a pure Kelvin-Helmholtz case. Similarly, as the shear increases the level of molecular mixing at the centerline also increases. This trend is the opposite of the previous cases

(Atwood number and modal comparison) where higher mixing widths had lower molecular mixing and vice versa.

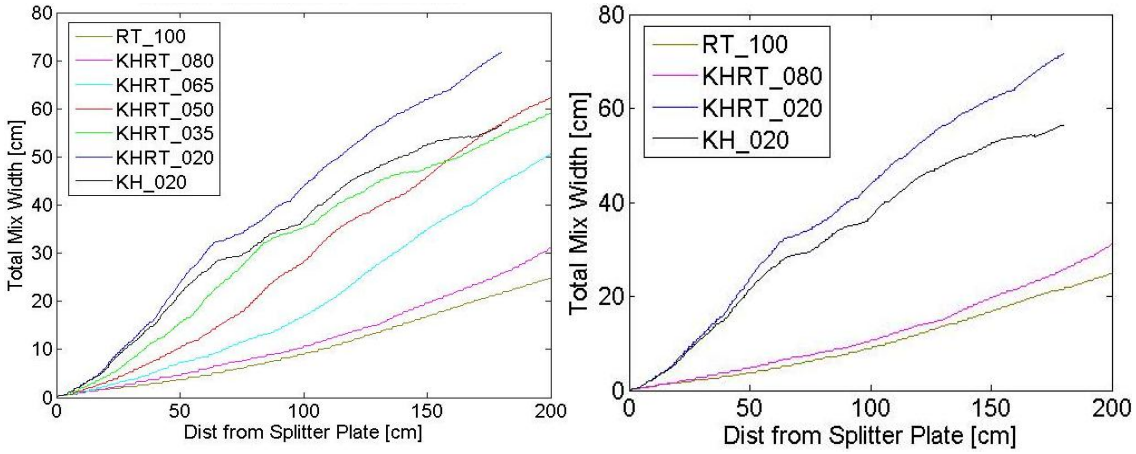

Figure 3.19. Mixing width for (left) pure Rayleigh-Taylor (RT_100), pure Kelvin-Helmholtz (KH_020), and five intermediate as described in Figure 3.18 and (right) pure Rayleigh-Taylor, pure Kelvin-Helmholtz, and minimum and maximum intermediate shears.

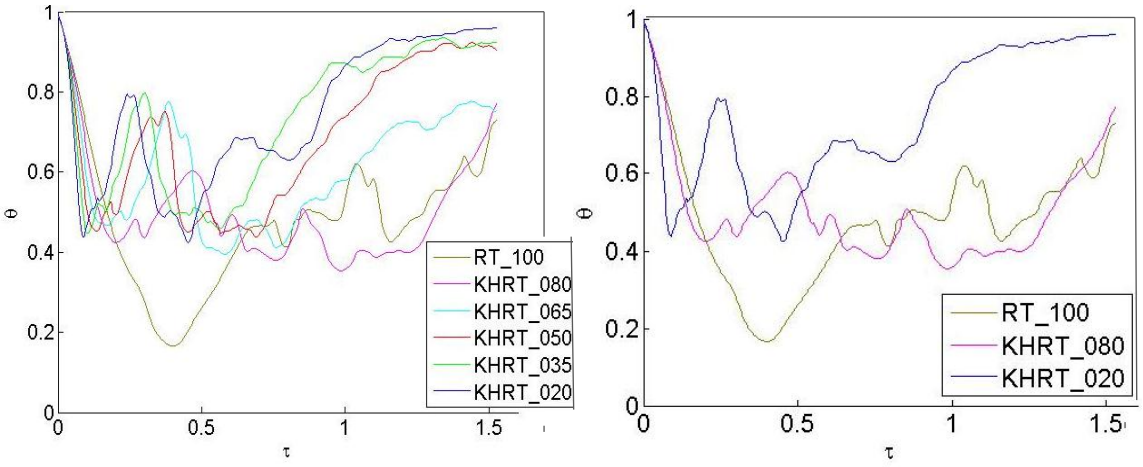

Figure 3.20. Level of molecular mixing at the centerline for (left) pure Rayleigh-Taylor (RT_100) and five intermediate as described in Figure 3.18.

The final way to compare the shear mixing is to investigate how the growth parameter α changes with the distance from the splitter plate (Figure 3.21). The values trend toward a quantity between 0.05 and 0.1, which matches well with experimental data and theory (Banerjee *et al.* 2010). The asymptotic value rises slightly with increased shear then lowers again, but always remains within the small range listed in other reports.

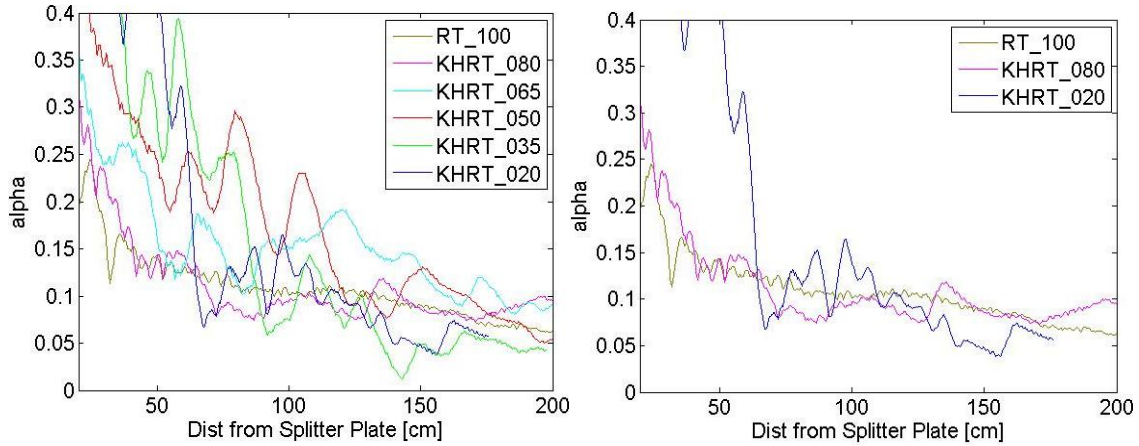

Figure 3.21. Growth parameter (left) pure Rayleigh-Taylor (RT_100) and five intermediate as described in Figure 3.18 and (right) pure Rayleigh-Taylor and minimum and maximum intermediate shears.

3.5 Comparison to Texas A&M University gas channel experiment

In order to prove the accuracy of the combined techniques listed in the previous section (density spectrum interface perturbation, initial velocity fluctuation, combine Rayleigh-Taylor and Kelvin-Helmholtz fluid instabilities, etc.), cases most similar to those considered in Akula *et al.* were compared.

3.5.1 Mixing width comparison

In Akula *et al.*'s work, three cases of combined shear and density instability were considered along with the pure Rayleigh-Taylor and pure Kelvin-Helmholtz instabilities mentioned earlier. All had an Atwood number of 0.035, similar to the computational run with Atwood number 0.032. KH+RT1 had shear of 0.23 m/s, similar to computational KHRT_080 with shear of 0.2 m/s; KH+RT2 had shear of 0.4 m/s, similar to computational KHRT_065 with shear of 0.35 m/s; KH+RT3 had shear of 0.62 m/s, similar to computational KHRT_035 with shear of 0.65 m/s. The mixing widths for both experiment and computation can be seen in Figure 3.22.

Looking at the trend of the two curves in (a), as more and more shear is added to the system, the experimental mixing width decreases but the computational mixing width increases. Looking at an early time outlook of the mixing width (b), the same trend can be seen. If instead the mixing widths are plotted against the equivalent time from the start of the instability, the two runs follow the same inclination of increased shear creating an increase in the mixing width. This difference can be explained by the conversion from time to space using the average velocity, which differs between the experimental and computational runs even though the shear match closely. For this reason, other methods of conversion need to be considered or time based comparisons should be used.

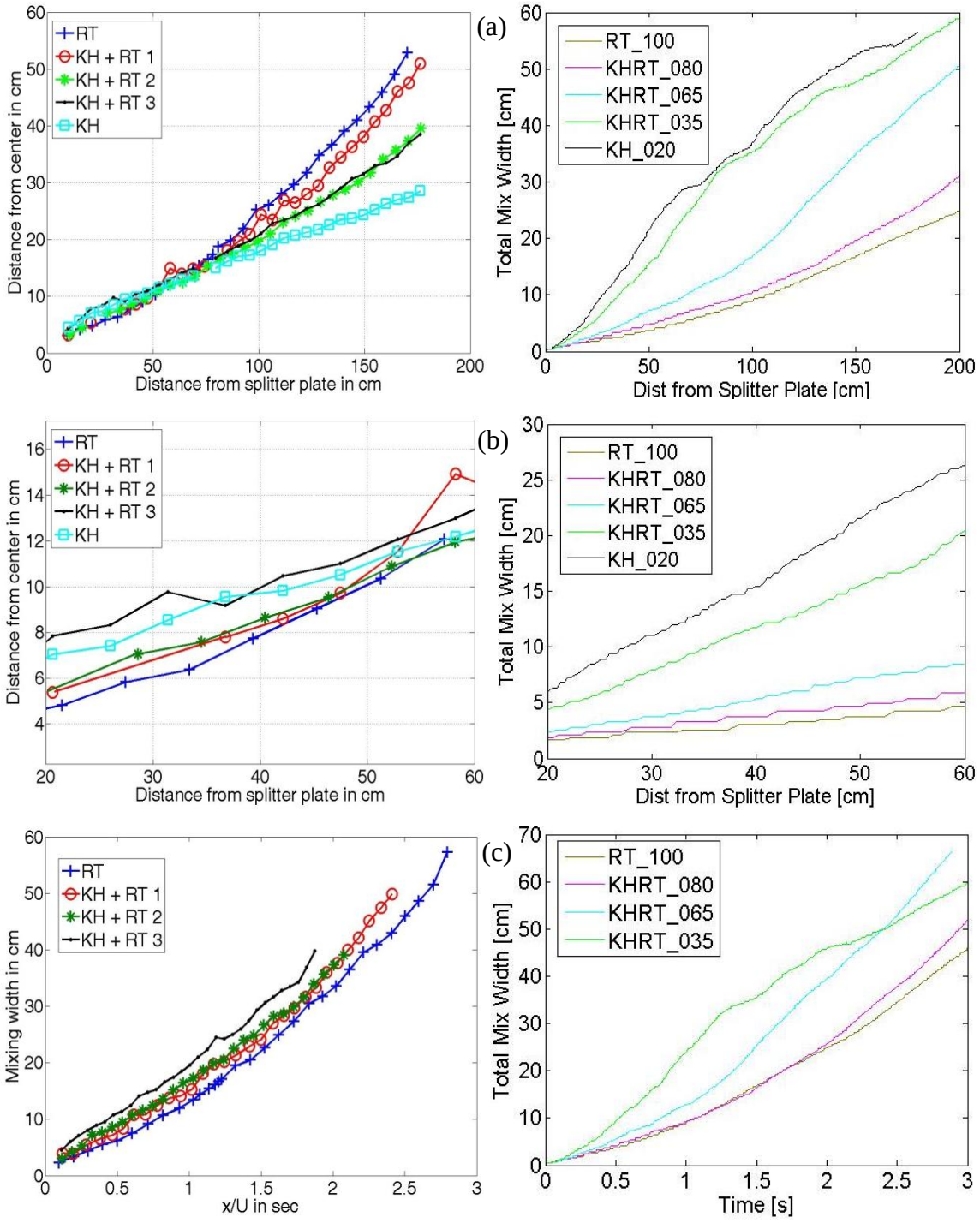

Figure 3.22. Mixing width comparison of experimental (left) and computational (right) run for (a) mixing width versus distance from splitter plate, (b) zoomed in section of mixing width versus distance, and (c) mixing width versus time from splitter plate.

3.5.2 Growth parameter comparison

Comparisons of the growth parameter for flows with density instabilities can provide insight into whether the rate of development of the computational code is operating correctly. Figure 3.23 shows a side by side comparison of the growth parameter for the pure Rayleigh-Taylor case as well as two of the combined shear instances. In the experiment, the growth parameter decreases with increased shear, but the computational code illustrates the opposite trend, instead increasing with the addition of shear. As this opposite inclination is the same as with the mixing width comparison, it is highly likely that a comparison of the growth parameter versus time from fluid interaction would provide results following the same track. However, in both experimental and computation cases, the growth parameter approaches a value between 0.05 and 0.1, which matches well with theory and previous experiments and provides further validity to the code's capabilities.

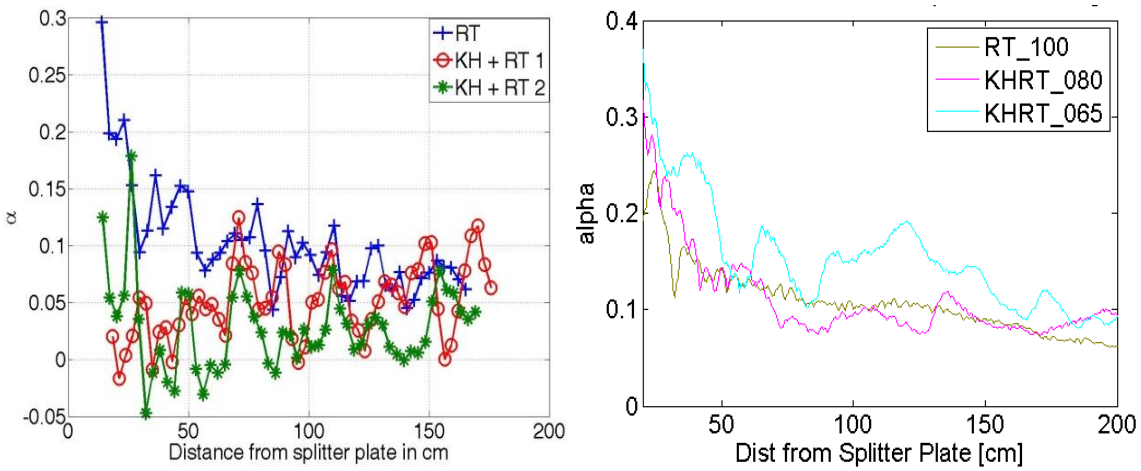

Figure 3.23. Growth parameter from experimental (left) and computational (right) run with legends as described in text and Figure 3.18.

3.5.3 Molecular mixing comparison

Another element to compare between the computational run and the experimental data is the level of molecular mixing at the centerline. Evaluation of Figure 3.24 shows similar elements between the two appraisal methods. At early nondimensionalized time, the order of mixing level is the same, namely as shear increases molecular mixing increases. As the time progresses, the values converge for all three levels of shear. In the experimental version, the three methods meet in the middle of the mixing levels that were observed prior to the convergence. For the computational data, the values are lower and thus all three techniques increase to their final assignment. The culmination value for both the experimental and computational cases are the same, around 0.75.

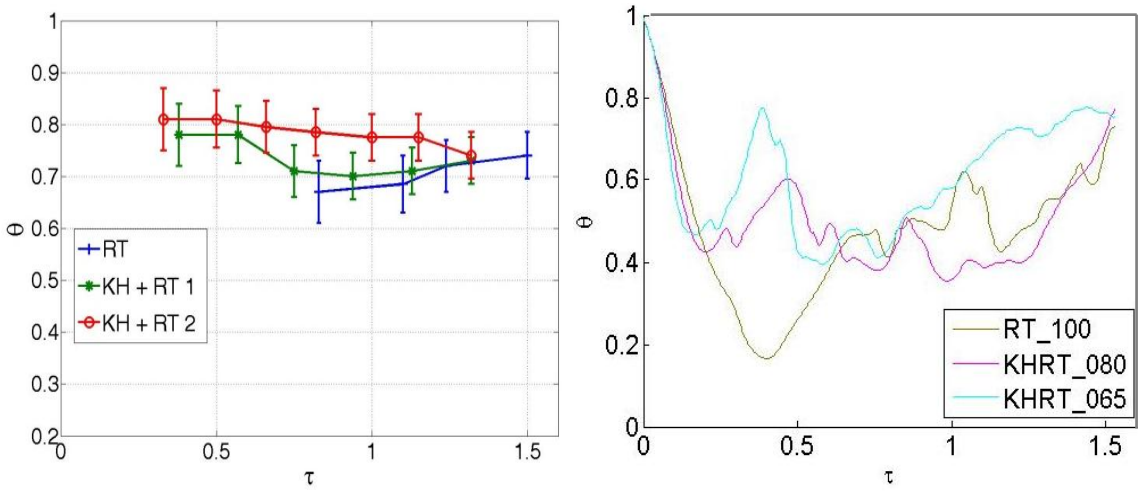

Figure 3.24. Level of molecular mixing at centerline for experiment (left) and computation (right) for pure Rayleigh-Taylor and combined shear-density instabilities.

3.5.4 Height gradient and the transitional Richardson number

The height gradient for the different levels of shear can be seen in Figure 3.25. Unlike the linear trend of the Rayleigh-Taylor height gradient (Figure 3.5) and the constant value height gradient of the Kelvin-Helmholtz instability (Figure 3.12), the height gradient with the combined instability has both linear and constant segments. As the shear in the system increases, the fraction of constant height gradient subsequently increases in both the experimental and computational varieties. This result makes sense theoretically as increased shear corresponds to a rise in Kelvin-Helmholtz effect, which is represented by a straight height gradient. Where the experiment and computation vary, however, is the location from the splitter plate where the transition from constant to linear height gradient occurs. The increased distance in the experiment, about 1.5 times the computational value, could be attributed to the difference in average velocity.

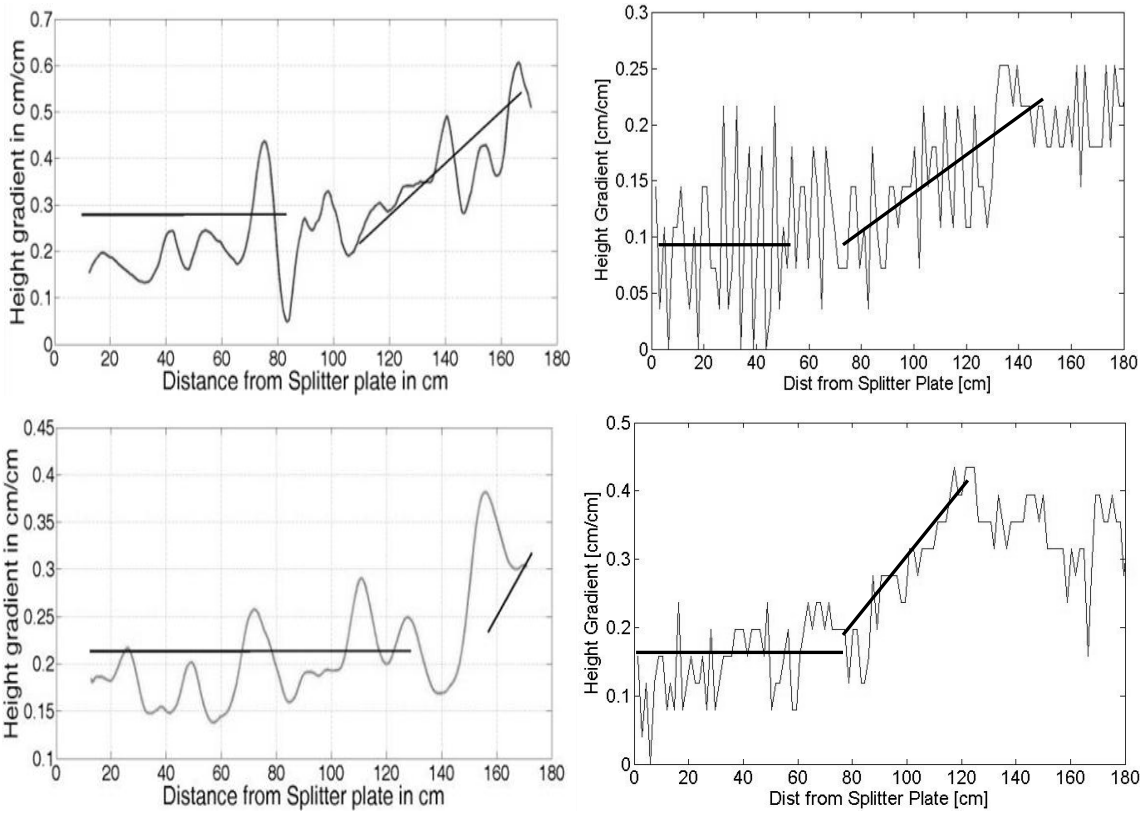

Figure 3.25. Height gradient of experimental (left) and computational (right) runs for (a) shear of 0.023 m/s and 0.2 m/s, respectively, and (b) shear of 0.4 m/s and 0.35 m/s, respectively.

Some believe the transition from the constant to linear trend occurs at a specific Richardson number, termed the transitional Richardson number. Comparing Figures 3.18 and 3.25, it can be seen that for the combined shear and density instabilities the transitional Richardson number ranges from -0.5 to -1. This value is lower than that of the experiment (-1.5 to -2.5); the difference can be described by the dependence of the Richardson number on the mixing width (equation 2.3). Since the mixing width of the experiment is larger than that of the computational run when compared versus the

distance from the splitter plate (Figure 3.22a), the Richardson number is consequently larger in the gas channel than the in the computational run.

3.5.5 Transitional Reynolds number

The final element to compare is the evolution of the Reynolds number as the shear in the system is increased. This value can be described as in equation (3.7) and in the mixing width as in (3.8).

$$\mathrm{Re} = \frac{2\mathrm{h}\mathrm{v}'}{\vartheta} \tag{3.7}$$

$$\mathrm{Re} = \frac{2\mathrm{h}^{3/2}}{\vartheta}\sqrt{\frac{\mathrm{gAt}}{3}} \tag{3.8}$$

where h is the total mixing width, v' is the velocity fluctuation, ϑ is the kinematic viscosity, g is gravity, and A_t is the Atwood number. As the shear in the system increases, the Reynolds number consequently increases (Figure 3.26). Because this value is directly dependent on the mixing width, which increases with shear, this is the trend that is expected. Looking at the transition from constant to linear growth of the height gradient (Figure 3.25) and relating it to the Reynolds number, the transition occurs at a range of 500 and 2900. The transitional range in the Akula *et al.* experiment occurs between 800 to 1500 which falls within the larger range found computationally.

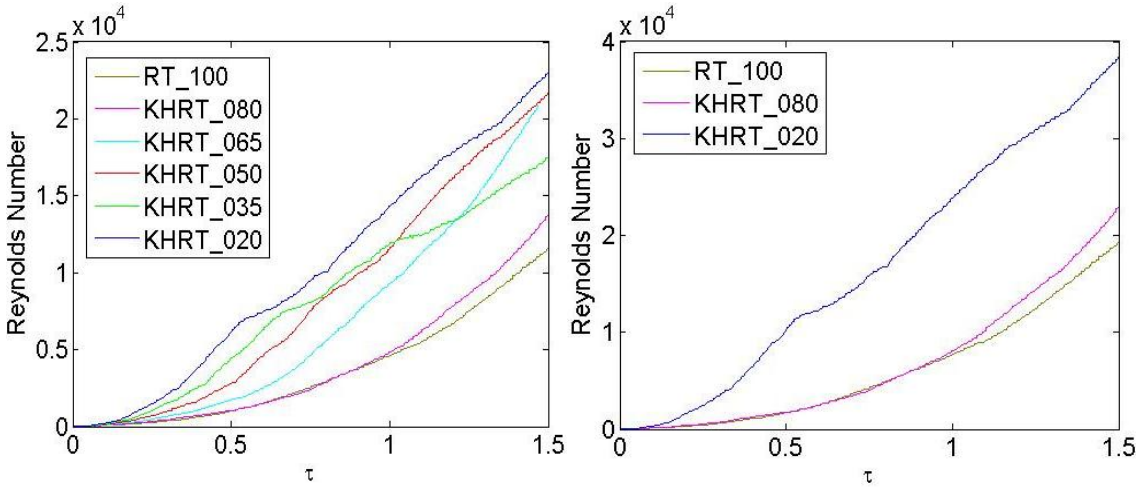

Figure 3.26. Reynolds number versus nondimensionalized time for (left) pure Rayleigh-Taylor (RT_100) and five intermediate shears as described in Figure 3.18 and (right) pure Rayleigh-Taylor and minimum and maximum intermediate shears.

4. CONCLUSIONS

4.1 Summary

This work utilized an implicit large eddy simulation code RTI3D under active development at Los Alamos National Laboratories and Texas A&M University to model numerous hydrodynamic instabilities. A summary of the accomplishments and conclusions from this work is provided below.

1. The computational code originally provided from Los Alamos National Laboratories was subsequently modified in order to have the capabilities necessary for modeling shear- and buoyancy-driven instabilities. Modifications include alteration of the fluid interface, assignment of initial conditions, adjustment of boundary conditions, and revision of velocity assignment methods, to name a few. The code was then validated using three published papers dealing with experimental Rayleigh-Taylor instabilities.
2. The effect of the Atwood number, and thus the level of density variation in the two fluids, was analyzed using identical setting excluding the density assignments for two cases based off of the gas channel experiment at Texas A&M University. One case had an Atwood number of 0.6 while the other a value of 0.032. Comparisons of mixing widths and level of molecular mixing at the centerline illustrated the low Atwood number case having a smaller mixing width but larger level of molecular mixing compared to its larger brethren.
3. To further improve the code's capabilities of replicating a physical experiment, investigation began on analyzing the spectrum of initial perturbation present at

the interface. A hot wire anemometer was used to obtain a power spectrum of the gas channel experiment, which was then utilized to create a multimode input perturbation for the code. Comparison of the results to the previous single mode case illustrated a larger mixing width but smaller molecular mixing with the density spectrum perturbation for the updated segment. This trend is the opposite of that seen with the low Atwood number, which was used for both modal components. The power spectrum data matched better with experimental data and theory and was thus used from there out.

4. While the code provided a closer match to experimental data with the modal increase, the Kelvin-Helmholtz instability replication was not completely accurate when compared to theory. It was determined that velocity fluctuations needed to be added to the system in order to spur the fluids into continual mixing, as the flow was lacking adequate input energy. The baseline fluctuation at the splitter plate was obtained from linear interpolation using two location measurements of the hot wire anemometer. Because the mixing growth in the vertical direction is most sensitive to vertical velocity fluctuations, three fractions of this component were also compared in order to determine which method provided the most accurate representation. The addition of velocity fluctuations provided the linear growth characteristic of shear based instabilities, and the full vertical fluctuation provided the closest match to experiment and theory for the mixing width and height gradient.

5. The combined Rayleigh-Taylor and Kelvin-Helmholtz instability was then investigated in order to both determine the abilities of the computational code as well as to understand the effect of shear on this compound driven flows. Five intermediate levels of shear transitioning between the pure Rayleigh-Taylor and pure Kelvin-Helmholtz instabilities mentioned earlier were explored. It was determined that increased shear resulted in a subsequent increased mixing width, which is to be expected due to the larger amount of energy in the system. As the shear in the system continued to rise, so did the level of molecular mixing at the centerline. Three specific cases of shear were compared to similar levels shown in experimental data from the Texas A&M gas channel. Mixing width, Richardson number, growth parameter, height gradient, and molecular mixing parameter all followed the same trends, thus proving the capabilities of the code and the accuracies of the work done.
6. Combining the information obtained above, namely that larger Atwood numbers and multiple modes are associated with larger mixing widths and less molecular mixing than their counterparts and that increased shear is associated with increased mixing width and molecular mixing, an optimal fuel pellet can be designed. The amount of shear in the system should be limited, and ideally none should be present. The multiple mode case combined with the small Atwood number provided a smaller level of molecular mixing than the single mode small Atwood number combination. This former setting should thus be aimed for through selection of fuels with very similar densities and through pellet

construction. It is important to note that the multimode assignment contained numerous perturbations (670 to be exact), so machining the inertial confinement fusion pellet with this level of undulations would be quite a task. Further, care must be taken if direct drive implosion techniques are used to ensure the distribution of the lasers' force as much as possible. This dissemination is important so as to avoid locations of concentrated energy which may create fewer modes with large amplitudes which would go against the optimal level of modes desired.

4.2 Sources of Error

Unlike experiments which rely heavily on equipment for data collection, and are thus reliant on the accuracies of these machines, computational investigation depends mainly on the computer upon which it is run. Still, there are numerous errors that can occur throughout the evaluation process.

1. The first potential source of error arises from the reliance on numerical dissipation to mimic viscosity in the evaluation of the fluid mixing. This process provides approximate dissipation and will not be identical to that seen in reality
2. The code is not capable to replicating inconsistencies between theory and nature. For instance, when modeling the magnetorheological fluid, in theory once the magnets are removed the fluid should begin to mix instantaneously. In reality, however, there is a residual magnetic impact and thus the mixing is delayed. In the code, the initial magnetic field is not modeled, while in nature there might be some residual field remaining which retards the growth at early time.

3. When the code is set to have velocity values as would be seen in nature rather than an inertial reference frame (such as top velocity 1 m/s, bottom velocity 0.5 m/s versus top velocity 0.25 m/s, bottom velocity -0.25 m/s, respectively), issues with advection arise. The cause for this error can be attributed to the fluid moving through more than one computational cell per time step due to the larger value of velocity. Running the code in the inertial reference frame helps fix the problem, but it is only a temporary patch to the problem. Further, there is still the potential for the advection issue to arise if the inertial reference frame velocity reaches a high enough value.
4. The last source of error described here, but certainly not the last source of error possible, is the fact that the code can only model up to 140 cm past the splitter plate when a density gradient is present. As mentioned earlier, the reason for this discrepancy is that the bubbles and spikes of the Rayleigh-Taylor instability saturate, causing the flow to transition from parabolic to linear growth. While this does not discredit the ability of the code to correctly model fluid mixing before this point, the capabilities are limited by only being able to analyze flows up to 140 cm.

4.3 Future Work

Based on the summary, conclusions, and sources of error, the following illustrates the future work to be done with the use of the computational code.

1. First and foremost, there are a number of corrections that need to be carried out on the code in order to better perfect its capabilities and expand its proficiencies.

The advection issue within the code needs to be permanently fixed rather than temporarily patched. Potential solutions include creating a method for grid refinement at trouble spots or simply putting in a test statement to insure the proper grid spacing for a given input velocity. Second, the saturation of bubbles and spikes in flows containing Rayleigh-Taylor instabilities needs to be resolved. Potential reasons for this issue include disagreement between velocity fluctuations of experiment and computation as well as inconsistencies in interface perturbations. This issue could also be affected by the advection issue mentioned previously.

2. The next path to take is to investigate the conversion from space to time when comparing experimental and computational works. While two methods can be compared as long as the relative shear between the two fluids is similar, the conversion process currently involves the average velocity. Ways in which to correct this is to model flows with similar shear and average velocity, or potentially look for a method of nondimensionalized time dealing with system conditions in order to avoid this issue.
3. As mentioned previously, Atwood number variations were compared, then modal components were compared. However, the arrangement of the two parameters in different combinations was not investigated. Testing of multimode interface perturbation with different Atwood numbers needs to be done in order to determine which trend wins out or if they simply combine. Namely, with

combined settings is the mixing width large and molecular mixing small, vice versa, or some combination of the two.

4. With the above information and that already obtained, the optimal density ratio could be obtained. It has already been determined that the shear should be minimal in the system, but as only two Atwood numbers were compared it is hard to draw conclusions for the density ratio as a whole. At least five other Atwood numbers should be compared and mixing widths and molecular mixing parameters plotted to observe the resulting trends.
5. While the multimode component was shown to be optimal over the single mode, there is the potential for an ideal number of modes, such that they combine and cancel each other out and minimize fluid mixing. Testing of alternative modal components should be done in order to determine the best perturbation for the successful implosion of an ICF capsule.

REFERENCES

Akula, B., Andrews, M., & Ranjan, D. 2012 The Effect of Shear on RT Mixing at Small Atwood Number. *Physical Review E* , awaiting submission.

Amerstorfer, U. V., Erkaev, N. V., Langmayr, D., & Biernat, H. K. 2007 On Kelvin–Helmholtz instability due to the Solar Wind Interaction with Unmagnetized Planets. *Planet. Space Sci.* **55**, 1811-1816.

Andrews, M. J. 1995. Accurate Computation of Convective Transport in Transient Two-Phase Flow. *Int. J. Numer. Methods Fluids* **21**, 205-222.

Azechi, H., Nakai, M., Shigemori, K., Miyanaga, N., Shiraga, H., Nishimura, H., Honda, M., Ishizaki, R., Wouchuk, J. G., Takabe, H., Nishihara, K., Mima, K., Nishiguchi, A., & Endo, T. 1997 Direct-Drive Hydrodynamic Instability Experiments on the GEKKO XII Laser. *Phys. Plasmas* **4**, 4079-4089.

Banerjee, A. & Andrews, M. J. 2006 Statistically Steady Measurements of Rayleigh-Taylor Mixing in a Gas Channel. *Phys. Fluids* **18**, 1-13.

Banerjee, A. & Andrews, M. J. 2009 3D Simulations to Investigate Initial Condition Effect on the Growth of Rayleigh-Taylor Mixing. *Int. J. Heat and Mass Trans.* **52**, 3906-3917.

Banerjee, A., Kraft. W. N., Andrews, M. J. 2010 Detailed Measurements of Statistically Steady Rayleigh-Taylor Mixing Layer from Small to High Atwood Number. *J. Flu. Mech.* **659**, 127-190.

Batchelor, G. K. 1967 *An Introduction to Fluid Dynamics.* Cambridge University Press, New York.

Baumgarten, C. 2006 *Mixture Formation in Internal Combustion Engines.* Springer-Verlag Berlin Heidelberg, Germany.

Bayvel, L. P. & Orzechowski, Z. 1993 *Liquid Atomization*. Taylor and Francis, Washington D.C.

Bernstein, I. B., & Book, D. L. 1978 Rayleigh-Taylor Instability of a Self-Similar Spherical Expansion. *Astrophysical Journal* **225**, 633-640.

Betti, R., Goncharov, V. N., McCrory, R. L., & Verdon, C. P. 1998 Growth Rates of the Ablative Rayleigh-Taylor Instability in Inertial Confinement Fusion. *Phys. Plasmas* **5**, 1446-1455.

Blaauwgeers, R., Eltsov, V. B., Eska, G., Finne, A. P., Haley, R. P., Krusius, M., Ruohio, J.J., Skrbek, L., & Volovik, G. E. 2002 Shear Flow and Kelvin-Helmholtz Instability in Superfluids. *Phys. Rev. Lett.* **89**, 1-4.

Blondin, J. M., Ellison, D. C. 2001 Rayleigh-Taylor Instabilities in Young Supernova Remnants Undergoing Efficient Particle Acceleration. *Astrophysical Journal* **560**, 244-253

Chandrasekhar, S. 1961 *Hydrodynamic and Hydromagnetic Stability*. Oxford University Press, New York.

Cheng, B. 2009 Review of Turbulent Mixing Models. *Acta Mathematica Scientia* **29**, 1703-1720.

Cook, A. W., Cabot, W., & Miller, P. L. 2004 The Mixing Transition in Rayleigh–Taylor Instability. *J. Fluid Mech.* **511**, 333-362.

Dalziel, S. B., Linden, P. F. & Youngs, D. L. 1999 Self-Similarity and Internal Structure of Turbulence Induced by Rayleigh-Taylor Instability. *J. Fluid Mech.* **399**, 1-48.

De Silva, I. P. D., Fernando, H. J. S., Eaton, F., & Hebert, D. 1996 Evolution of Kelvin-Helmholtz Billows in Nature and Laboratory. *Earth Planet. Sci. Lett.* **143**, 217-231.

Dimonte, G. & Schneider, M. 2000 Density Ratio Dependence of Rayleigh–Taylor Mixing for Sustained and Impulsive Acceleration Histories. *Phys. Fluids* **12**, 304-321.

Drazin, P. G. 2002 *Introduction to Hydrodynamic Stability*. Cambridge University Press, New York.

Duineveld, P. C. 2003 The Stability of Ink-Jet Printed Lines of Liquid with Zero Receding Contact Angle on a Homogeneous Substrate. *J. Flu. Mech.* **477**, 175-200.

Emery, M. H., Gardner, J. H., & Boris, J. P. 1982 Rayleigh-Taylor and Kelvin-Helmholtz Instabilities in Targets Accelerated by Laser Ablation. *Phys. Rev. Lett.* **48**, 677–680.

Emmons, H. W., Chang, C. T., & Watson, B. C. 1960 Taylor Instability of Finite Surface Waves. *J. Flu. Mech.* **7**, 177-193.

Fraschetti, F., Teyssier, R., Ballet, J., & Decourchelle, A. 2010 Simulation of the Growth of the 3D Rayleigh-Taylor Instability in Supernova Remnants Using an Expanding Reference Frame. *Astronomy and Astrophysics* **515**, 1-16.

Freed, N., Ofer, D., Shvarts, D., & Orszag, S. 1991 Two-Phase Flow Analysis of Self-Similar Turbulent Mixing by Rayleigh–Taylor Instability. *Phys. Fluids* **3**, 912-918.

Grinstein, F. F., Margolin, L.G., & Rider, W. J. 2007 *Implicit Large Eddy Simulation: Computing Turbulent Fluid Dynamics*. Cambridge University Press, New York.

Gutman, S. & Sivashinsky, G. I. 1990 The Cellular Nature of Hydrodynamic Flame Instability. *Physica D: Nonlinear Phenomena* **43**, 129-139.

Helmholtz, H. V. 1868 Über discontinuierliche Flüssigkeits-Bewegungen. *Monatsberichte der Königlichen Preussische Akademie der Wissenschaften zu Berlin* **23**, 215-228.

Hof, B., van Doorne, C. W. H., Westerweel, J., Niuwstadt, F. T. M., Faisst, H., Eckhardt, B., Wedin, H., Kerswell, R. R., & Waleffem, F. 2004 Experimental Observation of Nonlinear Traveling Waves in Turbulent Pipe Flow. *Science* **305**, 1594-1598.

Horton, W., Perez, J. C., Carter, T., & Bengtson, R. 2005 Vorticity Probes and the Characterization of Vortices in the Kelvin-Helmholtz Instability in the Large Plasma Device Experiment. *Phys. Plasmas* **12**, 1-8.

Ji, H., Burin, M. J., Schartman, E., Goodman, J. 2006 Hydrodynamic Turbulence Cannot Transport Angular Momentum Effectively in Astrophysical Disks. *Nature* **444**, 343-346.

Kadau, K., Barber, J. L., Germann, T. C., Holian, B. L., & Alder, B. J. 2010 Atomistic Methods in Fluid Simulation. *Phil. Trans. R. Soc. A* **368**, 1547-1560.

Keefe, D. 1982 Inertial Confinement Fusion. *Ann. Rev. Nucl. Part. Sci.* **32**, 391-441.

Kelvin, L. 1871 Hydrokinetic Solutions and Observations. *Phil Mag.* **42**, 362–377.

Kilkenny, J. D., Glendinning, S. G., Haan, S. W., Hammel, B. A., Lindl, J. D., Munro, D., Remington, B. A., & Weber, S. V. 1994 A Review of the Ablative Stabilization of the Rayleigh-Taylor Instability in Regimes Relevant to Inertial Confinement Fusion. *Phys. Plasmas* **1**, 1379-1389.

Kull, H. J. 1991 Theory of the Rayleigh-Taylor Instability. *Phys. Reports* **206**, 197-325.

Kuhlmann, H. C. & Rath, H. J. 1993 Hydrodynamic Instabilities in Cylindrical Thermocapillary Liquid Bridges. *J. Flu. Mech.* **247**, 247-274.

Lai, D., Rasio, F. A., & Shapiro, S. L. 1993 Hydrodynamic Instability and Coalescence of Binary Neutron Stars. *Astrophysical Journal* **420**, 811-829.

Lewis, D. J. 1950 The Instability of Liquid Surfaces when Accelerated in a Direction Perpendicular to their Planes II. *Proc. R. Soc. Lond. A* **202**, 81-96.

Lindl, J. 1995 Development of the Indirect-Drive Approach to Inertial Confinement Fusion and the Target Physics Basis for Ignition and Gain. *Phys. Plasmas* **2**, 3933-4024.

Lindl, J., McCrory, R. L., & Campbell, E. M. 1992 Progress Toward Ignition and Burn Propagation in Inertial Confinement. *Physics Today* **45**, 32-40.

Meyer-ter-Vehn, J., Atzeni, S., & Ramis, R. 1999 Inertial Confinement Fusion. *Europhysics News* **29**, 202-205.

Miles, J. W. 1957 On the Generation of Surface Waves by Shear Flows. *J. Flu. Mech.* **3**, 185-204.

Moin, P. & Mahesh, K. 1998 Direct Numerical Simulation: A Tool in Turbulence Research. *Annu. Rev. Fluid Mech.* **30**, 539–578.

Moseler, M. & Landman, U. 2000 Formation, Stability, and Breakup of Nanojets. *Science* **289**, 1165-1169.

Mueschke, N. J. 2008 *Experimental and Numerical Study of Molecular Mixing Dynamics in Rayleigh-Taylor Unstable Flows*. Ph.D. dissertation, Texas A&M University.

Ofman, L. & Thompson, B. J. 2011 Observation of Kelvin-Helmholtz Instability in the Solar Corona. *The Astrophysical Journal Letters* **734**, 1-5.

Olson, B. J., Larsson, J., Lele, S. K., & Cook, A. W. 2011 Nonlinear Effects in the Combined Rayleigh-Taylor/Kelvin-Helmholtz Instability. *Phys. Fluids* **23**, 1-10.

Oron, D., Alon, U., & Shvarts, D. 1998 Scaling Laws of the Rayleigh–Taylor Ablation Front Mixing Zone Evolution in Inertial Confinement Fusion. *Phys. Plasmas* **5**, 1467-1476.

Orszag, S. A. 1971 Accurate Solution of the Orr-Sommerfeld Stability Equation. *J. Flu. Mech.* **50**, 689-703.

Palmer, H. J. 1976 The Hydrodynamic Stability of Rapidly Evaporating Liquids at Reduced Pressure. *J. Flu. Mech.* **75**, 487-511.

Patnaik, P. C., Sherman, F. S., & Corcos, G. M. 1976 A Numerical Simulation of Kelvin-Helmholtz Waves of Finite Amplitude. *J. Flu. Mech.* **73**, 215-240.

Perri, F. & Cameron, A. G. W. 1974 Hydrodynamic Instability of the Solar Nebula in the Presence of a Planetary Core. *Icarus* **22**, 416-425.

Rayleigh, L. 1883 Investigation of the Character of the Equilibrium of an Incompressible Heavy Fluid of Variable Density. *Proc. London Math. Soc.* 14, 170-177.

Read, K. I. 1984 Experimental Investigation of Turbulent Mixing by Rayleigh-Taylor Instability. *Physica D: Nonlinear Phenomena* **12**, 45-58.

Remington, B. A., Weber, S. V., Haan, S. W., Kilkenny, J. D., Glendinning, S. G., Wallace, R. J., Goldstein, W. H., Wilson, B. G., & Nash, J. K. 1993 Laser-Driven Hydrodynamic Instability Experiments. *Phys. Fluids* **5**, 2589-2595.

Ristorcelli, J. R. & Clark, T. T. 2004 Rayleigh–Taylor Turbulence: Self-Similar Analysis and Direct Numerical Simulations. *J. Fluid Mech.* **507**, 213-253.

Scinocca, J. F. 1995 The Mixing of Mass and Momentum by Kelvin-Helmholtz Billows. *J. Atmos. Sci.* **52**, 2509-2530.

Shumlak, U. & Roderick, N. F. 1998 Mitigation of the Rayleigh–Taylor Instability by Sheared Axial Flows. *Phys. Plasmas* **5**, 2384-2389.

Sivashinsky, G. I. 1977 Nonlinear Analysis of Hydrodynamic Instability in Laminar Flames – I. Derication of Basic Equations. *Acta Astronautica* **4**, 1177-1206.

Sivashinsky, G. I. & Clavin, P. 1987 On the Nonlinear Theory of Hydrodynamic Instability in Flames. *J. Physique* **48**, 193-198.

Sharp, D. H. 1984 An Overview of Rayleigh-Taylor Instability. *Physica D: Nonlinear Phenomena* **12**, 3-18.

Smeeton, V. S. & Youngs, D. L. 1987 Experimental Investigation of Turbulent Mixing by Rayleigh-Taylor Instability. *Atomic Weapons Establishment* **35**, 1-71.

Snider, D. M. & Andrews, M. J. 1994 Rayleigh-Taylor and Shear Driven Mixing with an Unstable Thermal Stratification. *Phys. Fluids* **6**, 3324-3334.

Sternling, C. V. & Scriven, L. E. 1959 Interfacial Turbulence: Hydrodynamic Instability and the Marangoni Effect. *A.I.Ch.E. Journal* **5**, 514-523.

Tabak, M., Munro, D. H., & Lindl, J. D. 1990 Hydrodynamic Stability and the Direct Drive Approach to Laser Fusion. *Phys. Fluids* **2**, 1007-1014

Taylor, G. I. 1931 Effect of Variation in Density on the Stability of Superposed Streams of Fluid. *Proc. R. Soc. Lond. A* **132**, 499-523.

Taylor, G. I. 1950 The Instability of Liquid Surfaces when Accelerated in a Direction Perpendicular to their Planes. *Proc. Royal Soc. London* **201**, 192-196.

Van Leer, B. 1977. Toward the Ultimate Conservative Difference Scheme. IV. A New Approach to Numerical Convection. *J. Computational Physics* **23**, 1977.

Walker, A. D. M. 1981 The Kelvin-Helmholtz Instability in the Low-Latitude Boundary Layer. *Planet. Space Sci.* **29**, 1119-1133.

Wang, S. & Rusak, Z. 1996 On the Stability of an Axisymmetric Rotating Flow in a Pipe. *Phys. Fluids* **4**, 1007-1016.

White, J., Oakley, J., Anderson, M., & Bonazza, R. 2010 Experimental Measurements of the Nonlinear Rayleigh-Taylor Instability Using a Magnetorheological Fluid. *Phys. Rev.* **81**, 1-6.

Wilson, D. C., Cranfill, C. W., Christensen, C., Forster, R. A., Peterson, R. R., Hoffman, N. M., Pollak, G. D., Li, C. K., Séguin, F. H., Frenje, J. A., Petrasso, R. D., McKenty, P. W., Marshall, F. J., Glebov, V. Yu., Stoeckl, C., Schmid, G. J.,

Izumi, N., & Amendt, P. 2004 Multifluid Interpenetration Mixing in Directly Driven Inertial Confinement Fusion Capsule Implosions. *Phys. Plasmas* **11**, 2723-2728.

Woods, J. D. & Wiley, R. L. 1972 Billow Turbulence and Ocean Microstructure. *Deep Sea Research and Oceanographic Abstracts* **19**, 87-121.

Youngs, D. L. 1984 Numerical Simulation of Turbulent Mixing by Rayleigh-Taylor Instability. *Physica D: Nonlinear Phenomena* **12**, 32-44.

Zaleski, S. & Julien, P. 1992 Numerical Simulation of Rayleigh-Taylor Instability for Single and Multiple Salt Diapirs. *Tectonophysics* **206**, 55-69.

APPENDIX A

NOMENCLATURE

amp	amplitude
A_t	Atwood number
b	Calibration constant from hot wire anemometry
B0	Effect of mixing due to molecular diffusion
B2	Resulting condition if both fluids were immiscible
E	Voltage value from hot wire anemometry probe
f_1	Volume fraction of fluid one
f_2	Volume fraction of fluid two
g	Gravitational acceleration
h	Half of mixing width
H	Height of the gas channel
h_b	Width of mixing layer on bubble side of mixing layer
h_s	Width of mixing layer on spike side of mixing layer
ICF	Inertial confinement fusion
k	Wavenumber
M_k	Modal component at wavenumber k
P	Pressure
Re	Reynolds number
Ri	Richardson number
t	Time

t'	Time value used for normalization
x	Downstream distance
y	Distance into the gas channel
z	Vertical height within the gas channel
α	Growth parameter
α_b	Bubble growth parameter
α_s	Spike growth parameter
ΔU	Velocity difference between the two flow streams
$\Delta\rho$	Velocity difference between the two flow streams
η	Amplitude height
θ	Molecular mixing parameter
λ	Wavelength
ρ	Density at current location
ρ_1	Density of fluid one
ρ_2	Density of fluid two
$\bar{\rho}$	Average density between the two flow streams
τ	Nondimensionalized time used for modeling molecular mixing

VITA

Name:	Beth Ann Placette
Address:	Advanced Mixing and Shocktube Laboratory Texas A&M University College Station, Texas 77843-3123
Email Address:	beth350357@tamu.edu
Education:	B.S. Biomedical Engineering Texas A&M University College Station, Texas, 2010